Contents lists available at ScienceDirect

Arabian Journal of Chemistry

journal homepage: www.ksu.edu.sa

Original article

Oyster shell-modified lignite composite in globular shape as a low-cost adsorbent for the removal of Pb^{2+} and Cd^{2+} from AMD: Evaluation of adsorption properties and exploration of potential mechanisms

Wenbo An [a,b,*], Yifan Liu [a], He Chen [c], Qiqi Wang [a], Xuechun Hu [a], Junzhen Di [a]

[a] School of Civil Engineering, Liaoning Technical University, Fuxin 123000, China
[b] School of Mining Engineering, China University of Mining and Technology, Xuzhou 221000, China
[c] School of Mechanics and Engineering, Liaoning Technical University, Fuxin 123000, China

ARTICLE INFO

Keywords:
Acid mine drainage
Lignite
Oyster shell
Synthesis
Adsorption-condensation
Heavy metal pollution

ABSTRACT

A low-cost composite adsorption material has been synthesized from fishery wastes and natural minerals to address challenges such as ecological balance destruction caused by high concentrations of Pb and Cd in acid mine drainage (AMD), unreasonable use of low-caloric lignite, and environmental pollution caused by idle accumulation of oyster shells. This new adsorbent can effectively treat AMD by improving acidity and adsorbing Pb^{2+} and Cd^{2+}. In this study, oyster shell-modified lignite composite in globular shape (OSL-G) was synthesized by using pyrolyzed oyster shell and lignite, with the addition of bentonite adhesive. The adsorption properties of OSL-G on AMD were evaluated, and the potential mechanism of OSL-G repairing AMD was explored. The results showed that when the mass ratio of oyster shell to lignite was 1:1, oyster shell-modified lignite composite (OSL) was synthesized at 900 °C for 20 min. When the adhesive content was 15.50 %, the roasting temperature was 640 °C, and the roasting time was 2.35 h, OSL-G was synthesized and the adsorption effect was the best. The OSL-G could effectively treat AMD with pH 4 ~ 5 and initial Pb^{2+} and Cd^{2+} concentrations of 10 mg/L within 600 min at a dosage of 4 g/L. The OSL-G adsorption process followed the quasi-second-order kinetic model and the Freundlich model. The maximum adsorption saturation capacities of Pb^{2+} and Cd^{2+} were 107.2821 mg/g and 8.3777 mg/g at 298.15 K, respectively. The adsorption process was a multistep controlled spontaneous endothermic process. The potential mechanism was mainly the adsorption-condensation coexistence results of electrostatic adsorption, neutralization precipitation, ion exchange, and surface complexation. The removal rates of Pb^{2+} and Cd^{2+} of the recovered OSL-G (ROSL-G) were still high, reaching 57.26 % and 50.38 % after 5 times of adsorption–desorption, respectively. The applicability of ROSL-G after adsorption–desorption for other heavy metal components in AMD proved its good application potential. This study suggested that OSL-G can be used as a promising environmentally friendly adsorbent for AMD. This study provided a broad picture of the management and reuse possibilities of fishery wastes and natural mineral resources, and addressed established, current, and potential strategic needs, particularly in terms of sustainability challenges and ecological civilization construction.

1. Introduction

AMD Acid mine drainage (AMD) is usually in the process of mineral mining, produced by the oxidation of sulfur-containing minerals in contact with air or water oxygen. Among the 14 large mineral resource production bases of 100 million tons in China, 11 of them are facing serious water shortages. Among them, Shaanxi, Gansu, Ningxia, Shanxi, Inner Mongolia, and other western coal base output reached more than 70 % of the national total coal production, but the water resources accounted for only 3.9 % of the national total (Zhang et al., 2023a,b). The discharge of mine wastewater accounts for about 10 % of the total industrial wastewater discharge in China. Among them, AMD is the most widely polluted and harmful (Liphadzi and Vermaak, 2017). Its acidity is high, the pH is generally between 2 and 4, a few can reach 6, and

* Corresponding author at: 88 Yulong Road, Xihe District, Fuxin City, Liaoning Province 123000, China.
E-mail addresses: WB_An1992@163.com (W. An), 2142561738@qq.com (Y. Liu), LNTUCH0903@163.com (H. Chen), 1403584935@qq.com (Q. Wang), xuechunhu45@126.com (X. Hu), dijunzhen@lntu.edu.cns (J. Di).

https://doi.org/10.1016/j.arabjc.2024.105732
Received 30 October 2023; Accepted 13 March 2024
Available online 17 March 2024

contains Fe, Mn, Cu, Zn, Pb, Cd and other heavy metals (Rodríguez-Galán et al., 2019; Akinwekomi et al., 2020). Pb and Cd are non-essential elements for the human body and are highly toxic, both of which will cause irreversible damage to the human body (Du et al., 2022). Therefore, it is necessary to further research on the treatment of Pb and Cd in AMD, to prevent or reduce their harm to the environment and human health.

At present, the conventional treatment technologies of AMD include neutralization and adsorption methods. The neutralization method with the addition of an alkaline neutralizer is a popular water treatment method (Alakangas et al., 2013). The process of this method is simple and low-cost, but it also faces the problems of difficult follow-up treatment of reaction products and easy to cause secondary pollution (Maree et al., 2013; Iakovleva et al., 2015). The adsorption method is widely recognized as the most effective technology for wastewater treatment, which has the advantages of wide sources, various types, low cost, high treatment efficiency, and convenient operation (Melo et al., 2015; Zendelska et al., 2018; Lee et al., 2022). The low-cost adsorbent materials include biological adsorbent materials (Znad et al., 2022), polymer adsorbent materials (Upadhyay et al., 2021), natural mineral adsorbent materials (Zhang et al., 2021; Cheng et al., 2023a,b), and industrial and agricultural solid waste adsorbent materials (Zhou et al., 2022; Zhang et al., 2022). The adsorption material is crucial for the adsorption method used to treat wastewater. It is of utmost importance to discover new adsorption materials that are efficient, affordable, and readily available. The future of AMD treatment lies in the development of environmentally friendly and cost-effective adsorption materials. Because AMD pollution is composed of complex and diverse components, dealing with it is challenging. Depending on a single material or treatment technology to address AMD has limitations. In water treatment processes, it is common to combine two or more treatment methods and materials to improve the capacity to treat water pollutants (Ren et al., 2022; Nkuna et al., 2023). With this in mind, this study aims to develop a composite material that combines the benefits of adsorption and neutralization methods to effectively treat AMD.

Lignite, a natural mineral product, is abundant and widely distributed in China. It has a rich specific surface area and a well-developed pore structure, providing numerous adsorption sites for heavy metal ions (Jellali et al., 2021). In addition, the inherent structure of lignite often contains a significant amount of active oxygen-containing groups (Mlayah et al., 2021). This characteristic imparts weak acidity, hydrophilicity, and excellent cation exchange capacity to lignite, enabling it to engage in complex physical and chemical adsorption reactions with heavy metal ions. Bao et al. (2021) selected 200 mesh lignite to treat 800 mg/L AMD, and the saturated adsorption capacities of lignite for Zn^{2+} and Cu^{2+} in AMD were 55.5 mg/g and 67.84 mg/g, respectively. Natural lignite as an adsorbent for the treatment of AMD has the advantages of economy, easy availability, and excellent effect. However, considering the adsorption capacity, adsorption selectivity, and neutralizing acidity of the adsorbent, the actual application of lignite is often modified, processed with other materials, or combined with aluminum salt, iron salt, and other flocculants to improve its adsorption capacity. Huang et al. (2019) conducted a study in which they treated lignite with nitric acid. The results showed that the pore size of the lignite increased, while the specific surface area decreased. In addition, the treatment led to an increase in polar oxygen-containing functional groups such as hydroxyl, carboxyl, and carbonyl groups on the surface, as well as the introduction of nitro groups. These changes enhanced the surface electronegativity, polarity, and hydrophilicity of lignite. The adsorption capacity of Pb^{2+} for lignite increased from 14.45 mg/g to 30.68 mg/g after the treatment. Wang et al. (2022) produced calcium-modified lignite-derived humin (Ca-CHM) by Ca(OH)(2) and used it for the adsorption and removal of Cd^{2+}. The weak aliphatic polarity and strong aromatic polarity of Ca-CHM were favorable for the adsorption of Cd^{2+}, and the maximum adsorption capacity of Ca-CHM for Cd^{2+} was 41.84 mg/g.

Oyster is a kind of Marine biological resource in the world, which has high economic value. The edible part is mainly processed, and the oyster shells are discarded or landfilled, leading to environmental pollution and resource waste (Tudor et al., 2006; Tamjidi and Ameri, 2020). The composition of oyster shell is composed of calcium-dominated minerals and organic matter, and the structure of oyster shell is an ordered multi-microlayer structure formed by the self-assembly of calcium carbonate on the macromolecular framework of organic matter. The surface of oyster shells is porous, rich in $CaCO_3$ and CaO, alkaline, and has good potential to neutralize acid and absorb heavy metals (Hsu, 2009; Bai et al., 2023). Xu et al. (2019) used oyster shell powder as a heavy metal adsorption material to compare its adsorption effects on Cu, Cd, and Pb in a single system and a co-existing system. The results showed that the order of adsorption capacity of oyster shell powder for the three metals in any system was Cu > Pb > Cd. Yen and Li (2015) applied the Taguchi method to remove Ni(II) by calcined oyster shell powders (OSP). When the optimum calcined temperature of OSP is 900 °C, the Ni(II) can be removed almost completely. The greater the calcination temperature, the higher the adsorption capacity. This is due to the large number of porosities created at the calcination temperature of 900 °C. The porosities generate a large amount of cavities which significantly increase the surface area for adsorption. Studies have shown that the high-temperature treatment of oyster shells will decompose the carbonate components into more alkaline CaO, which is accompanied by the escape of CO_2, which is conducive to enhancing its alkalinity release ability and increasing its porosity, but at the same time will lead to the increase of the agglomeration of oyster shell powder. Shi et al. (2022) loaded iron-manganese oxide (FMBO) on calcined oyster shells by hydrothermal method to prepare FMBO/OS composite material, which not only solved the defects of difficult separation and easy agglomeration of FMBO particles but also effectively adsorbed and removed As(III) in water. Therefore, oyster shells can be combined with other natural mineral materials that have good potential for water treatment. This combination allows for the advantages of both adsorption materials to be utilized, addressing the limitation of using a single adsorption material for pollutant treatment and enhancing overall water treatment capacity (Zhou et al., 2022; Liu et al., 2023).

The main purpose of this study is to develop a new low-cost composite adsorbent for the treatment of AMD containing Pb^{2+} and Cd^{2+} by combining the advantages of neutralization and adsorption. This adsorbent is synthesized by using natural minerals (lignite) with a good heavy metal adsorption effect as the carrier, loaded with marine solid wastes (oyster shells) that can release alkalinity. The optimum preparation conditions of OSL-G were determined through batch experiments to achieve the best adsorption capacity and application potential. The adsorption properties of OSL-G were evaluated and the potential mechanism was explored. The use of OSL-G as an adsorbent highlights its broad prospects for AMD remediation. The novelty aspect of this study is to find a new solution for the treatment of AMD. Meanwhile, it can alleviate the environmental pressure caused by oyster shells and the unreasonable use of low-caloric lignite. Moreover, it can achieve the purpose of treating waste of waste, practicing the concept of green mine development, and responding to the strategic needs of ecological civilization construction.

2. Materials and methods

2.1. Materials, chemicals, and simulated AMD

The lignite used in this experiment was obtained from Shanxi Fuhong Mineral Products Co., LTD (Shanxi, China). It was thoroughly cleansed with deionized water, dried at 105 °C in a blast drying oven for 24 h, and subsequently crushed to 80 ~ 100 mesh using a high-speed grinder. Finally, it was screened, and saved for later. The oyster shells used in this experiment were purchased from a market in Fuxin City, Liaoning Province, China. To exclude the influence of other factors, the residual

impurities on the surface of oyster shells should be removed and cleaned with deionized water several times. Then placed them in a blast drying oven at 105 °C for 48 h. Once naturally cooled, they were crushed with a high-speed grinder until the particle size was 100 ~ 200 mesh, then screened, and saved for later. The bentonite used in this experiment was calcium bentonite purchased from Shanlinshiyu Mineral Products Company (Hunan, China).

All chemical reagents are analytically pure and have not been further purified. HNO_3 was purchased from Shenyang Huadong Reagent Factory (Shenyang, China), $Pb(NO_3)_2$, $Cd(NO_3)_2$ and NaOH was purchased from Liaoning Quanrui Reagent Co., LTD. (Shanghai, China). All glassware is soaked in HNO_3 (10 %) solution for at least 24 h and then ultrasonic cleaned. After repeated wetting with deionized water, then dried in a constant temperature oven for later use.

The concentration range of pollutants(Pb, Cd) in the mine water of a Mining Co., Ltd. in Huludao, Liaoning Province, China was taken as a reference (Table 1). $Pb(NO_3)_2$ and $Cd(NO_3)_2$ were used as raw materials to prepare simulated AMD containing Pb^{2+} and Cd^{2+}. Its water quality index was $C_0(Pb^{2+}) = 50$ mg/L, $C_0(Cd^{2+}) = 10$ mg/L, pH = 4. Adjust the pH value by adding 0.1 M of HNO_3 or 0.1 M of NaOH solution. All experimental water samples were used in the current configuration and are not retained.

2.2. Preparation of OSL-G composites

The preparation process of OSL-G consists of three parts. First, the prepared 5 g oyster shells with a diameter of 100 ~ 200 mesh were put into the crucible tongs and pyrolyzed in the muffle furnace. The pyrolysis temperature was set as 750 °C, 800 °C, 850 °C, 900 °C, 950 °C, and 1000 °C, and the pyrolysis time was set as 10 min, 20 min, 30 min, 60 min, 90 min, and 120 min. The pyrolyzed oyster shells were immersed in 250 mL deionized water and treated with ultrasound for 1.5 h to obtain the pyrolyzed oyster shell suspension. Second, the lignite with a particle size of 80 ~ 100 mesh was added to the suspension, the mass ratio of lignite to oyster shells was set as 1:3, 1:2, 1:1, 2:1 and 3:1, and the mixture was stirred in a constant temperature magnetic stirrers at 800 rpm for 6 h at room temperature to obtain the mixture. The mixture was transferred to an oven at 105 °C for drying to remove water, and (x, y, z) OSL composites were obtained, where x was the pyrolysis temperature of oyster shells, y was the pyrolysis time of oyster shells, and z was the mass ratio of lignite to oyster shells. Third, the OSL composites and bentonite adhesive (the content was 0 %, 5 %, 10 %, 15 %, 20 %, and 30 %) were added to a certain amount of deionized water, so neither hard nor soft was appropriate, repeatedly and fully kneaded to uniform, by squeezing the ball method made of about 3 ~ 5 mm balls and sealed aged for 12 h. The aged pellets were put into the crucible tongs, and placed in the muffle furnace preheated to 250 °C, then heated to a certain temperature (400 °C, 500 °C, 600 °C, 700 °C, and 800 °C) and roasted for a while (0.5 h, 1 h, 1.5 h, 2 h, and 2.5 h). After taking out, the pellets were cooled naturally to obtain (x, y, z) OSL-G composites. Where x was the adhesive content, y was the roasting temperature, and z was the roasting time.

2.3. Batch experiments

The adsorption behavior of Pb^{2+} and Cd^{2+} by (x,y,z) OSL and (x,y,z) OSL-G composites was studied in batches at room temperature. 0.2 g/L (x,y,z) OSL and 4 g/L (x,y,z)OSL-G were added to 50 mg/L Pb^{2+} and 10 mg/L Cd^{2+} simulated solutions with pH = 4, respectively, and adsorbed in a 150 rpm thermostatic oscillator for 24 h. After the reaction, the samples were removed by pipetting gun and filtered by 0.45 μm microporous membrane. The residual concentrations of Pb^{2+} and Cd^{2+} in the simulated solutions were measured under different preparation conditions (pyrolysis temperature of oyster shells, pyrolysis time of oyster shells, mass ratio of lignite to oyster shells, adhesive content, roasting temperature, and roasting time), and the removal rate (R_e) and adsorption capacity (q_e) were calculated by Eqs. (A.1) and (A.2).

Based on the above single-factor test, a three-factor, three-level Response Surface Methodology (RSM) was designed using the Box Behnken Design (BBD) model. The adhesive content (A, %), roasting temperature (B, °C), and roasting time (C, h) were selected as the variables. The removal rate of Pb^{2+}, the removal rate of Cd^{2+}, the loss rate of OSL-G, and the pH after reaction were taken as the response values. The interaction between the three factors and further optimization of the preparation conditions was analyzed. In this experiment, a total of 17 groups of experiments were designed. Design-expert 8.0 software was used to carry out fitting analysis on the experimental data, and the quadratic response regression equation between each variable and the response value was obtained. Moreover, Fisher's statistical test was used for the analysis of variance (ANOVA) to obtain the interaction between the variable and the response value, and to evaluate the quality of "goodness of fit".

The OSL-G obtained under the above optimum preparation conditions was selected for subsequent adsorption experiments. The effects of different factors (adsorbent dosage, initial pH, initial concentration, and binary metal system) on the adsorption of Pb^{2+} and Cd^{2+} by OSL-G were investigated. Batch experiments were conducted at room temperature and in a 150 mL conical flask at 150 rpm. The effect of adsorbent dosage (1 g/L, 2 g/L, 3 g/L, 4 g/L, 5 g/L, and 6 g/L) on the adsorption of Pb^{2+} and Cd^{2+} by OSL-G was studied. The effect of initial pH (2, 3, 4, 5, and 6) on the adsorption of Pb^{2+} and Cd^{2+} by OSL-G was studied by adjusting the pH with 0.1 M HNO_3 solution. The effect of initial concentration of Pb^{2+} and Cd^{2+} (10 mg/L, 30 mg/L, 50 mg/L, 70 mg/L, 100 mg/L, pH = 4) on the adsorption by OSL-G at different temperature systems (15 °C, 25 °C, and 35 °C) was investigated. Pb^{2+} and Cd^{2+} coexist in AMD, so it is necessary to set up binary competitive adsorption experiments. The adsorption effect of Pb^{2+} and Cd^{2+} by OSL-G in a binary metal system was investigated, and the binary competition between non-equal amounts of Pb^{2+} and Cd^{2+} was investigated. The Pb-Cd mixture was configured (in which the concentration of Cd^{2+} was 10 mg/L, and the concentration of Pb^{2+} was 10 mg/L, 30 mg/L, 50 mg/L, 70 mg/L and 100 mg/L, respectively, pH = 4). The Cd-Pb mixture was configured (in which the concentration of Pb^{2+} was 50 mg/L, and the concentration of $Cd^{2+}$was 10 mg/L, 30 mg/L, 50 mg/L, 70 mg/L and 100 mg/L, respectively, pH = 4).

The adsorption kinetics, adsorption isotherm, and thermodynamic

Table 1
Actual Water Quality of Mine Water in a Mining Co., Ltd. in Huludao (2018–2022).

Actual Water Quality of Mine Water in a Mining Co., Ltd. in Huludao (2018–2022)									
Year	pH			Pb^{2+} (mg/L)			Cd^{2+} (mg/L)		
	Minimum	Mean	Maximum	Minimum	Mean	Maximum	Minimum	Mean	Maximum
2018	2.12	4.51	5.47	20.57	47.15	55.36	2.87	9.52	15.48
2019	2.11	4.03	5.33	18.65	44.58	50.24	3.89	9.87	12.54
2020	2.36	3.49	6.14	35.14	55.24	75.45	4.36	11.27	16.25
2021	2.14	3.69	6.02	30.78	52.36	70.56	5.24	10.56	17.52
2022	2.45	3.85	5.89	22.65	48.23	50.50	2.66	9.45	12.69
Average value	—	3.91	—	—	49.51	—	—	10.13	—

behaviors of Pb^{2+} and Cd^{2+} were studied at different initial mass concentrations (10 mg/L, 30 mg/L, and 50 mg/L) and temperatures (288.15 K, 298.15 K, and 308.15 K). Pseudo-first-order kinetics, pseudo-second-order kinetics, and intra-particle diffusion kinetics were used to fit the adsorption kinetic data of Pb^{2+} and Cd^{2+} by OSL-G. The fitting models are shown in Eqs. (A.3)–(A.5). Langmuir model and Freundlich model were used to fit the adsorption isotherm data of Pb^{2+} and Cd^{2+} by OSL-G. The fitting models are shown in Eqs. (A.6) and (A.7). Gibbs free energy ΔG, entropy change ΔH, and enthalpy change ΔS were used to describe the thermodynamic behavior of Pb^{2+} and Cd^{2+} by OSL-G. The thermodynamic parameters are shown in Eqs. (A.8)–(A.10).

2.4. Regeneration and application of ROSL-G

In the regeneration experiment, the adsorbed and saturated ROSL-G containing Pb^{2+} and Cd^{2+} were washed several times with deionized water and dried in an oven at 80 °C for 24 h. The 4 g/L dried ROSL-G was added to the desorption solution of 100 mL 1 M NaOH, 0.1 M NaOH, H_2O, 1 M HNO_3, and 0.1 M HNO_3, respectively. Oscillate in a shaker at 150 rpm at 30 °C for 12 h. The concentrations of Pb^{2+} and Cd^{2+} in the solution were measured, and the desorption rate was calculated by Eq. (A.11). To explore the reusability of ROSL-G, the above optimal desorption solution was selected for subsequent reuse experiments. The separated ROSL-G was washed with deionized water to remove the desorption solution and dried in an oven at 50 °C for 24 h to determine the adsorption capacity of the recovered adsorbent for Pb^{2+} and Cd^{2+}. After adsorption, ROSL-G was added to the optimal desorption solution again, and the second adsorption–desorption cycle experiment was carried out, and a total of 5 adsorption–desorption cycles were carried out in the experiment.

The toxicity characteristic leaching procedure (TCLP) was carried out for evaluating heavy metal-leachability of adsorbent after 5 cycles. 10 g of sample was put into a polypropylene bottle with 200 mL of leachant (0.1 M of CH_3COOH, pH = 2.8, demineralized water) added (Pan et al., 2020). Then the polypropylene bottle was shocked at 40 rpm in a rotary agitator at 25 °C for 20 h. After extraction, the leachate was filtered and acidified to pH < 2 with HNO_3, and then detected the concentrations of Pb^{2+} and Cd^{2+}.

Due to the complex heavy metal components of AMD, ROSL-G after adsorption–desorption was tried to be used for the adsorption of other metal ions to investigate its applicability. The 4 g/L ROSL-G after adsorption–desorption was added to the solution of Pb^{2+}, Cd^{2+}, TFe, Mn^{2+}, Cu^{2+}, Zn^{2+}, and Cr^{6+} with the pH value was 4 and the concentration was 50 mg/L, respectively. Then the residual metal ion content in the water was measured.

The real AMD samples used in this experiment were taken from the tailings wastewater of a lead–zinc mine in Huludao City, Liaoning Province, China. Samples were collected in 5-litre polypropylene bottles, carried at a constant temperature of 4 °C, and tested on the day of collection. The removal rate of 0.4 g OSL-G to heavy metals (Pb, Cd, Fe, Mn, Cu, and Zn) and anion (SO_4^{2-}) in real AMD was determined. The reaction condition to keeping consistent with the adsorption experiment.

2.5. Characterization and analytical methods

The surface area (S_{BET}), total pore volume (V_{tot}), and pore size distribution of the materials were evaluated using the micromeritics ASAP2020 N_2 adsorption/desorption instrument (BET, Micromeritics, USA). The surface morphology of the materials was characterized by Regulus 8100 scanning electron microscope (SEM, Hitachi, Japan) and Ultra Dry Energy dispersive X-ray (EDS) spectroscopy. The Bruker D8 advance X-ray diffractometer (XRD, Bruker, Germany) was used to determine the crystal structure and relative content changes in the samples. The changes of functional groups of the materials were characterized by Bruker ALPHA II Fourier infrared spectroscopy (FTIR, Bruker, Germany).

The pH value in wastewater was determined by the glass electrode method (GB/T 6920-86). Heavy metal ions (Pb^{2+}, Cd^{2+}, Zn^{2+}, Cu^{2+}) concentrations were measured through an atomic absorption spectrometer method (GB 7475-87). The wavelengths used for the analysis of the Pb^{2+}, Cd^{2+}, Zn^{2+}, and Cu^{2+} were 283.3, 228.8, 213.8, and 324.7 nm, respectively. Heavy metal ions (TFe and Mn^{2+}) were determined by the flame atomic absorption spectrophotometry method (GB 11911-89). The wavelengths used for the analysis of the TFe, and Mn^{2+} were 248.3, and 279.5 nm, respectively. Heavy metal ion (Cr^{6+}) was determined by Dtphenylcarbohydrazide spectrophotometric method (GB 7467-87). The wavelengths used for the analysis of the Cr^{6+} were 540 nm.

2.6. Statistical analysis

All figures were drawn using the Origin 2018 software (Origin Lab Corp.). All the kinetic and isotherm models were fitted using non-linear fitting function. All significant differences were reported at 0.05 probability level and all experimental data were presented as mean values ± standard deviations. Design-expert 8.0 software was used to carry out fitting analysis on the RSM experimental data. Fisher's statistical test was used for the analysis of variance (ANOVA) to evaluate the quality of "goodness of fit".

3. Results and discussion

3.1. Optimization of preparation conditions on OSL and OSL-G

3.1.1. Preparation conditions of OSL

In Fig. 1(a), it is evident that the pyrolysis temperature of oyster shells played a crucial role in the removal of Pb^{2+} and Cd^{2+} by OSL. The removal rate and adsorption capacity of both pollutants increased significantly within the temperature range of 750 °C to 900 °C. At 900 °C, the removal rate of Pb^{2+} and Cd^{2+} reached 98.92 % and 99.08 %, respectively, and the adsorption capacity was 247.3 mg/g, and 49.54 mg/g, respectively. Although the removal rate and adsorption capacity slightly increased within the temperature range of 900 °C to 1000 °C, the increase was not significant. The presence of organic matrix in oyster shells may affect its pyrolysis temperature, but the content of organic matrix in oyster shells is relatively low, less than 5 %, so it is negligible (Xu et al., 2021). Oyster shell powder has the characteristics of a large surface area, small particle size, and rich porous structure, which reduces the thermal stability of calcite structure. The reasons for this phenomenon are as follows: Firstly, oyster shells, which are rich in $CaCO_3$, decompose into CaO after high-temperature pyrolysis. This process is accompanied by a large amount of CO_2 gas escaping, resulting in the transformation of the layered structure of oyster shells into a new porous structure with a large specific surface area. This increases the contact area between the main component CaO and water and heavy metals (Xu et al., 2019). Secondly, CaO has a strong electrostatic affinity for hydroxyl functional groups at its coordination position, making it easy to hydrolyze and complexly react with heavy metal ions. As a result, heavy metals can be removed (Shi et al., 2022). Thirdly, after ultrasonic treatment, a portion of CaO is hydrolyzed and converted to Ca$(OH)_2$. Ca$(OH)_2$ plays a role in activating and expanding the pores of lignite during the agitated impregnation process, introducing more hydroxyl and other functional groups on the surface of lignite, and improving the pore structure of lignite. This greatly enhances the ability of lignite to adsorb heavy metal ions (Moon et al., 2013; Zhong et al., 2021). Ha et al. (2019) found that the $CaCO_3$ and CaO contents of Taean and Tongyeong oyster shells were different when the pyrolysis temperature was between 700 °C and 1000 °C. Due to the difference in organic matter content, fineness, and calcite texture, the pyrolysis temperature of oyster shells in different regions is also different. Combined with the results of this experiment and previous studies, it was speculated that the pyrolysis of oyster shells used in this experiment at

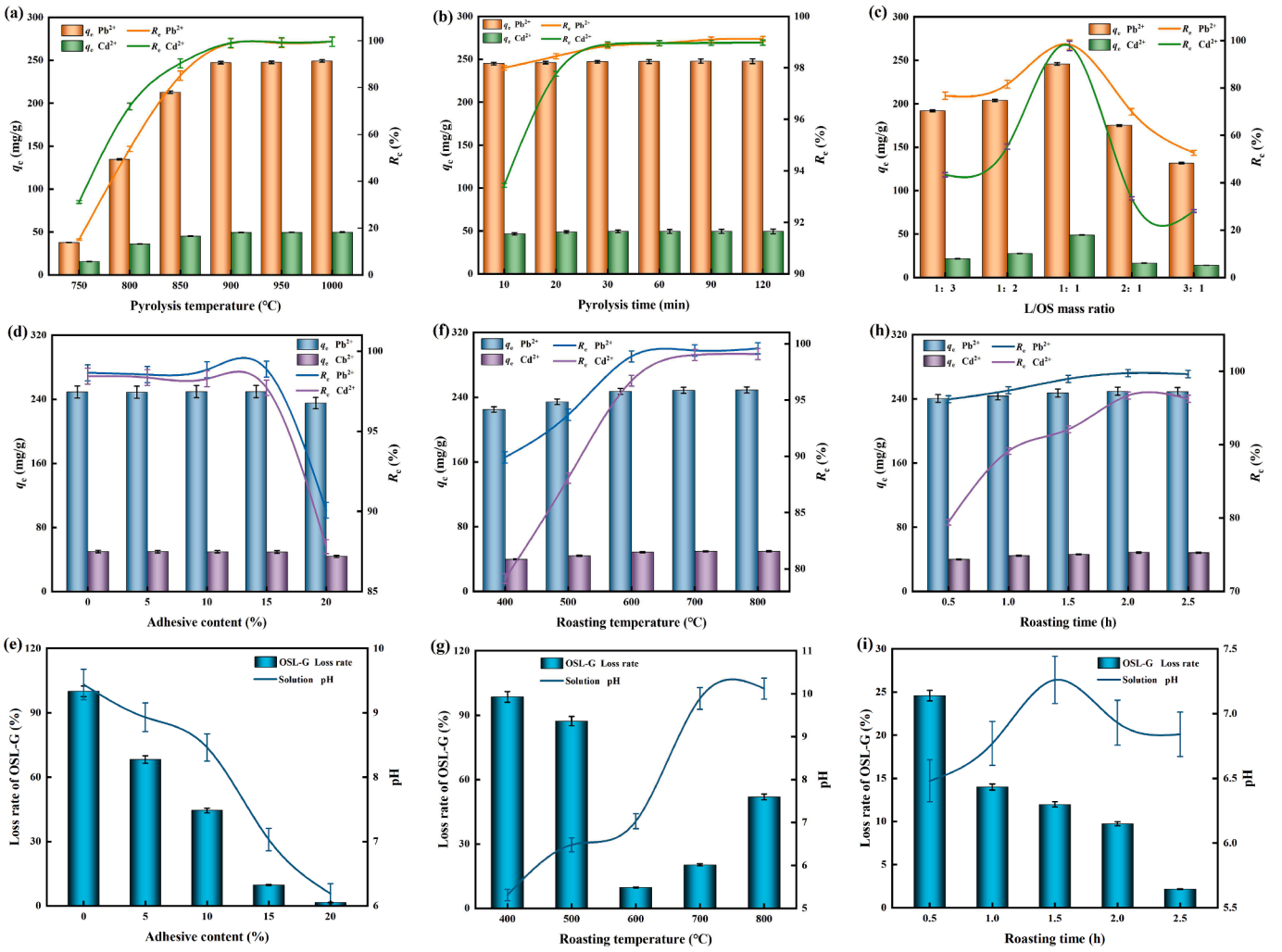

Fig. 1. The preparation conditions (a) pyrolysis temperature, (b) pyrolysis time, (c) L/OS mass ratio of OSL and the preparation conditions (d and e) adhesive content, (f and g) roasting temperature, (h and i) roasting time of OSL-G.

900 °C achieved a large amount of decomposition of the calcite structure, lost CO_2, and transformed into CaO, which was also confirmed by Suwannasingha et al. (2022). The pyrolysis temperature of 900 °C was chosen for OSL preparation.

In Fig. 1(b), the removal rates and adsorption capacity of Pb^{2+} and Cd^{2+} by OSL increase as the pyrolysis time of oyster shells goes from 10 min to 20 min. However, there is no significant change in the removal rates and adsorption capacity when the pyrolysis time is further increased after 20 min. This suggests that the decomposition of oyster shells starts at 10 min and is mostly finished by 20 min. During this process, a majority of calcite is transformed into CaO. These findings are consistent with the results obtained by Xia et al. (2021). According to Alidoust et al. (2015), the diameter of oyster shells is not expected to decrease regardless of the pyrolysis temperature. However, an increase in pyrolysis time leads to the recrystallization of particles, resulting in larger particle sizes and reduced surface area. This, in turn, hinders the hydration of CaO to produce $Ca(OH)_2$, thereby reducing the effectiveness of OSL in removing Pb^{2+} and Cd^{2+}. To prevent crystal aggregation after pyrolysis, ultrasonic shear treatment is recommended. To minimize energy consumption and processing costs during subsequent ultrasonic treatment, while ensuring the adsorption performance of OSL for Pb^{2+} and Cd^{2+} in AMD. The pyrolysis time of 20 min was chosen for OSL preparation.

In Fig. 1(c), when the mass ratio of lignite to oyster shells is 1:1, the removal rates and adsorption capacity of Pb^{2+} and Cd^{2+} by OSL are the highest, achieving 99.36 % and 100 %, 248.4 mg/g and 50 mg/g, respectively. As the proportion of oyster shells increased, the removal effect decreased. On one hand, the alkalinity and solubility of oyster shells are enhanced after undergoing pyrolysis and ultrasonic treatment. However, excessive loading of lignite can lead to an excessive amount of –OH on the surface of OSL, which accelerates the dissolution rate. Consequently, when metal ions in an aqueous solution come into contact with the OSL surface, they quickly precipitate and generate a significant amount of hydroxide. This, in turn, leads to substantial precipitation and accumulation on the OSL surface, ultimately blocking the pores of composite materials and hindering the adsorption reaction. On the other hand, oyster shells hold a significant quantity of Ca^{2+}. The inclusion of suitable Ca^{2+} in OSL facilitates the ion exchange process with Pb^{2+} and Cd^{2+} in solution, effectively eliminating them (Khan et al., 2018; Madrid and Lanzon, 2017). Nevertheless, an excessive cation content on OSL generates repulsion towards heavy metal ions in solution, hindering their proximity to OSL (Li et al., 2015; Lu et al., 2018). Consequently, the adsorption capability of OSL on Pb^{2+} and Cd^{2+} is influenced. The mass ratio of lignite to oyster shells was 1:1 to prepare OSL.

3.1.2. *Preparation conditions of OSL-G*

The excellent properties of adsorbed materials not only depend on the adsorption effect but also consider their recyclability and secondary pollution problems. With this in mind, a spherical composite material, OSL-G, was prepared by using lignite and oyster shell as the substrate

and adding bentonite as the binder. The composite material can release alkalinity slowly, and solve the problem of large dispersion and difficult separation and recovery of powdering adsorption material. Bentonite is a kind of natural clay mineral with good adhesion, plasticity, non-toxicity, and thermal stability. After roasting with lignite powder and oyster shell powder, a volcanic ash reaction will occur, resulting in the formation of stable and durable calcium silicate hydrate (C-S-H) or calcium aluminosilicate hydrate (C-A-S-H) (Zhan et al., 2020; Bai et al., 2021). This facilitates the slow release of alkalinity and the effective removal of Pb^{2+} and Cd^{2+} in AMD. Sun et al. (2020) found that the generation of hydration products decelerates the release rate of alkalinity, but too much gel would reduce the permeability of the material after hardening. The adhesive content plays a crucial role in determining the removal rate of Pb^{2+} and Cd^{2+}, the loss rate of OSL-G, and the pH in AMD. In Fig. 1(d and e), it is evident that the removal rate and adsorption capacity of Pb^{2+} and Cd^{2+}, the loss rate of OSL-G, and the pH of the solution system all decreased as the adhesive content increased. When the adhesive content was 15 %, the loss rate of OSL-G decreased to 9.74 %, while the removal rates and adsorption capacity of Pb^{2+} and Cd^{2+} remained at 99.87 %, and 96.71 %, 12.48 mg/g, and 2.42 mg/g, respectively. In addition, the pH of the solution system increased from 4 to 6.93 after the reaction. Under this condition, OSL-G can not only maintain a high removal rate of Pb^{2+} and Cd^{2+}, but also ensure the strength of particles, and the pH of the reaction solution system can reach the emission standard. OSL-G was prepared with a selected adhesive content of 15 %.

After extruding the lignite and oyster shell powder with 15 % adhesive, roasting them at a specific temperature can enhance the strength of the particles and improve the balance force between them. Additionally, this process can also enhance the ability of the OSL-G composite to release alkalinity. Fig. 1(f and g) shows that the loss rate of OSL-G decreases significantly with the increase of roasting temperature in the range of 400 °C ~ 600 °C. However, the loss rate increases with the increase of roasting temperature after 600 °C. According to the research results of Bai et al. (2021), when the roasting temperature rises from 400 °C to 500 °C, some SiO_2 in the material preferably transforms into an amorphous state and reacts to form C-S-H and other hydrates. Hydrate makes OSL-G have a certain mechanical strength, but its loss rate is still high due to insufficient production. The roasting temperature gradually increased from 500 °C to 600 °C, and SiO_2 and other Al and Si compounds in a large number of materials reacted with calcium oxides in oyster shells to form gel products C-S-H, C-A-S-H, etc., which was conducive to enhancing the strength of OSL-G (Okano et al., 2013; Alastair et al., 2018). As the temperature continued to rise, the gel product transformed into a crystalline phase, and the higher the temperature, the higher the crystallinity. However, the crystallization of the gel products C-S-H and C-A-S-H will cause the binding force between the materials to decrease, resulting in the loss rate increasing again. In addition, roasting will lead to material moisture loss and will lead to brown coal and oyster shell powder decomposition to produce CO_2 gas. The loss of water vapor and the escape of CO_2 gas will cause the porosity of OSL-G. The higher the roasting temperature, the faster the water vapor dissipation, and the stronger the decomposition reaction, resulting in excessive pores of OSL-G, the collapse of pore structure, and the decrease of mechanical strength. It can also be seen from Fig. 1(f and g) that with the increase in roasting temperature, the removal rate of Pb^{2+} by OSL-G fluctuates slightly but maintains a high state, while the removal rate of Cd^{2+} and the pH of the solution system obviously increase first and then tends to equilibrium. Roasting causes the decomposition of $CaCO_3$ in oyster shell powder, resulting in the formation of CaO. This increases the alkalinity of OSL-G. The addition of OSL-G to a solution helps raise its pH, facilitating the precipitation of Pb^{2+} and Cd^{2+} and ultimately achieving a higher removal rate. The likelihood of the $CaCO_3$ decomposition reaction occurring increases with higher calcination temperatures. However, as the temperature increases, the CaO and its hydrolyzed products react with the silicate and silica aluminate precursors in the material, leading to the formation of gelling substances. Excessive gelling products can then block the pore structure of the adsorbent material (Mo et al., 2018), impacting the removal of Pb^{2+} and Cd^{2+}. OSL-G was prepared at a temperature of 600 °C.

In Fig. 1(h and i) it is evident that with the increase of roasting time, the loss rate of OSL-G decreases. This is because the extension of roasting time is not only conducive to the decomposition of $CaCO_3$ of oyster shells into CaO but also conducive to the full reaction among Ca, Al, and Si oxides to generate cementation products, thus enhancing the mechanical strength of OSL-G. It can also be seen from Fig. 1(h and i) that the removal rates and adsorption capacity of Pb^{2+} and Cd^{2+} by OSL-G increased first and then decreased with the increase of roasting time, and the pH of the solution system also has the same trend. During the roasting process, the production of silicate and silica aluminate compounds is insufficient to meet cementation requirements within the 0.5 h to 1.5 h timeframe. However, extending the roasting time in this range has two positive effects. Firstly, it promotes the formation of more alkaline CaO. Secondly, it facilitates the evaporation of water molecules and the volatilization of CO_2 gas, which is a decomposition product of organic matter and carbonate. This leads to an increase in the pore size of the adsorbed material. Consequently, a short-term increase in roasting time enhances the capacity for alkalinity release, resulting in an improved removal rate of Pb^{2+} and Cd^{2+}. When the roasting time reaches 2 h, further increasing it will result in excessive cementation products of OSL-G and increased crystallinity. This, in turn, will make it difficult to release alkalinity, ultimately reducing the removal rate of Pb^{2+} and Cd^{2+}. Comparatively, the solubility product constant of Cd^{2+} precipitate is smaller than that of Pb^{2+}, making the removal of Cd^{2+} more influenced by the alkalinity of the solution system. Consequently, the adsorption effect of OSL-G on Cd^{2+} undergoes a more significant change with variations in roasting temperature. OSL-G was prepared with a roasting time of 2 h.

3.1.3. Optimize preparation conditions of OSL-G by RSM

The BBD levels, test design, and responses are shown in Table B1. Response surface regression analysis was performed on the experimental results using Design Expert V8.0.6 software. Quadratic regression equations were established between the adhesive content (A), roasting temperature (B), roasting time (C) of the independent variable and the removal rate of Pb^{2+} (Y_1), the removal rate of Cd^{2+} (Y_2), the loss rate of OSL-G (Y_3), and pH value of the solution (Y_4), as shown in Eqs. (1)–(4).

$$Y_1 = 99.87 - 0.057A + 0.024B + 0.014C - 0.033AB + 0.022AC + 0.01BC + 0.018A^2 - 0.06B^2 - 0.039C^2 \quad (1)$$

$$Y_2 = 96.71 - 3.93A + 2.52B - 0.31C + 0.57AB - 0.99AC + 0.21BC - 3.19A^2 + 0.56B^2 - 0.026C^2 \quad (2)$$

$$Y_3 = 5.74 - 16.76A - 22.79B - 6.12C + 0.21AB + 4.75AC - 4.23BC + 4.82A^2 + 50.04B^2 + 10.41C^2 \quad (3)$$

$$Y_4 = 6.76 - 0.51A + 1.11B - 0.23C - 0.22AB + 0.05AC - 0.14BC + 0.13A^2 + 1.15B^2 + 0.033C^2 \quad (4)$$

Analysis of variance (ANOVA) was performed on the above quadratic regression equation to determine the accuracy of the model and the significance of the influence of various factors and their interactions on the response value. The results are shown in Tables B2–B5. The significance of the model is determined by both the F-value and P-value. The larger the F-value is and the smaller the P-value is, the more significant the impact will be. The F values of the regression models from Y_1 to Y_4 are 26.29, 109.88, 243.27, and 181.06, respectively. The P values of these models are all < 0.0001, and their lack of fit is 0.8347, 0.6903, 0.1551, and 0.105, respectively. It shows that the model has high reliability, the model reaches a significant level, has statistical significance, and can be used to analyze the results of the actual point of the test (Mousavi et al., 2018; Luo et al., 2021). In addition, if the P-value of

primary terms A, B, and C of the model is less than 0.05, it indicates that the three factors A, B, and C have significant influence on the response value, and vice versa. If the P-values of the secondary interaction terms AB, AC, and BC of the model meet the significance requirement, it indicates that the interaction effect between the secondary interaction terms is significant (Zhang et al., 2023a,b). The R^2 of each model is 0.9713, 0.9930, 0.9968, 0.9957, which is very close to 1, indicating that the regression model has a high degree of fit. In addition, the accuracy of the experiment was tested by three coefficients, namely, $R^2_{Adj} - R^2_{Pred} < 0.2$, coefficient of variation (C.V.) < 10 %, and Adeq Precision (AP) > 4. If all the requirements were met, the accuracy, reliability, and precision of the experiment could be considered to be high (Kacakgil and Cetintas, 2021; Saeed et al., 2021). Hence, the aforementioned regression models effectively describe the response values $Y_1 \sim Y_4$, making them suitable for analysis, prediction, and optimization purposes. In the Pb^{2+} removal rate model, F values of A, B, and C were 100.35, 17.12, and 5.74, and P values were <0.0001, 0.0044, and 0.0478, respectively. The results showed that the adhesive content had a significant effect on the removal rate of Pb^{2+}. The significant degree was the adhesive content > roasting temperature > roasting time. Similarly, in the other three models, the influence of adhesive content and roasting temperature on the removal rate of Cd^{2+}, the loss rate of OSL-G, and the pH of the solution was found to be highly significant. The significant degree was the adhesive content > roasting temperature > roasting time.

To comprehensively consider the influence of three factors A, B, and C on the response value, a graphical analysis was carried out, and the three-dimensional response surface map was shown in Fig. 2. It can be seen from Fig. 2(a), in the Pb^{2+} removal rate model, the contours of the interaction between AB and AC present a long oval shape with long axis, indicating that the interaction effect between AB and AC is significant. The distribution density of the contours on the X-axis is significantly higher than that on the Y-axis, indicating that the main effect of A is larger than that of B and C. However, the interaction between B and C is not significant, showing that the contour map presents a circular distribution, and the three-dimensional response surface map is steeper. Similarly, it can be seen from Fig. 2(b) that the same results are also obtained in the Cd^{2+} removal rate model. It can be seen from Fig. 2(c) that in the loss rate model, the interaction of AB is not significant, while the interaction of AC and BC is significant. It can be seen from Fig. 2(d) that in the pH value model, the interaction between AB and BC is significant, while the interaction between AC is not. The results of ANOVA also fully verified the above conclusions.

To prepare OSL-G composite with good adsorption effect of Pb^{2+} and Cd^{2+} and low loss rate, the Design expert V8.0.6 software was used to optimize the preparation method of OSL-G composite. The results showed that the optimum preparation conditions of OSL-G composites were as follows: the adhesive content was 15.48 %, the roasting temperature was 642 °C, and the roasting time was 2.37 h. It is predicted that the removal rate of Pb^{2+} and Cd^{2+} were 99.89 % and 99.02 %, the loss rate was 9.87 %, and the pH of the solution was 7.49. Considering the feasibility and economic cost of the experiment, some adjustments were made to the experimental results. The optimum preparation conditions of OSL-G were determined the adhesive content was 15.50 %, the roasting temperature was 640 °C, and the roasting time was 2.35 h.

3.2. Characteristics of OSL and OSL-G

The removal effect of adsorbents on the removal rates and adsorption capacity of Pb^{2+} and Cd^{2+} are shown in Fig. 3(a). It can be seen from Fig. 3(a), that the removal rates of Pb^{2+} and Cd^{2+} by OSL were 98.93 % and 99.76 %, respectively, and the adsorption capacity of Pb^{2+} and Cd^{2+} were 247.33 mg/g, 49.88 mg/g, respectively. Compared with single lignite or oyster shell material, the removal rates were significantly improved, which was 1.67 times (Pb^{2+}) and 2.23 times (Cd^{2+}) for single

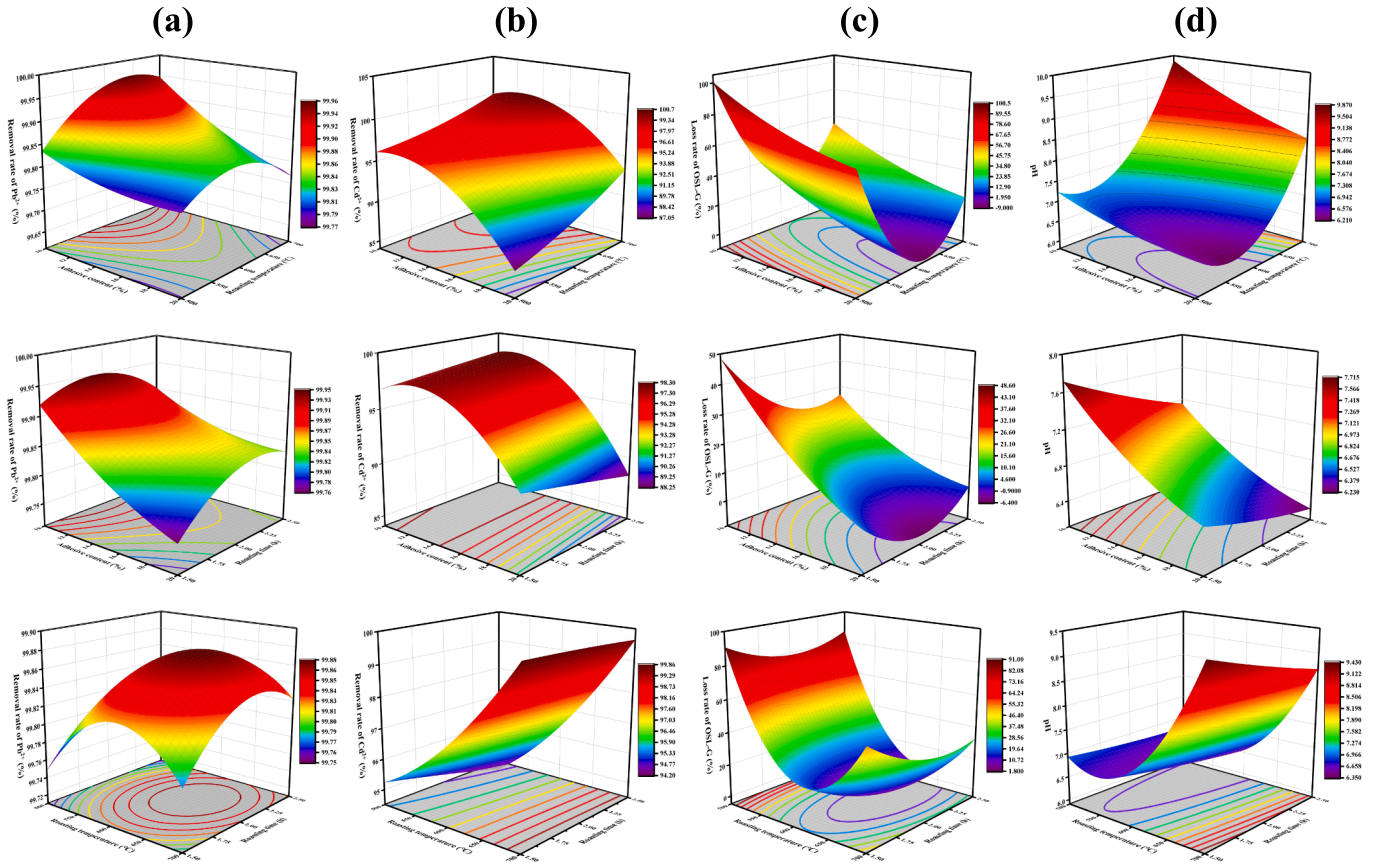

Fig. 2. The three-dimensional response surface maps of (a) removal rate of Pb^{2+}, (b) removal rate of Cd^{2+}, (c) loss rate of OSL-G, (d) pH of the solution.

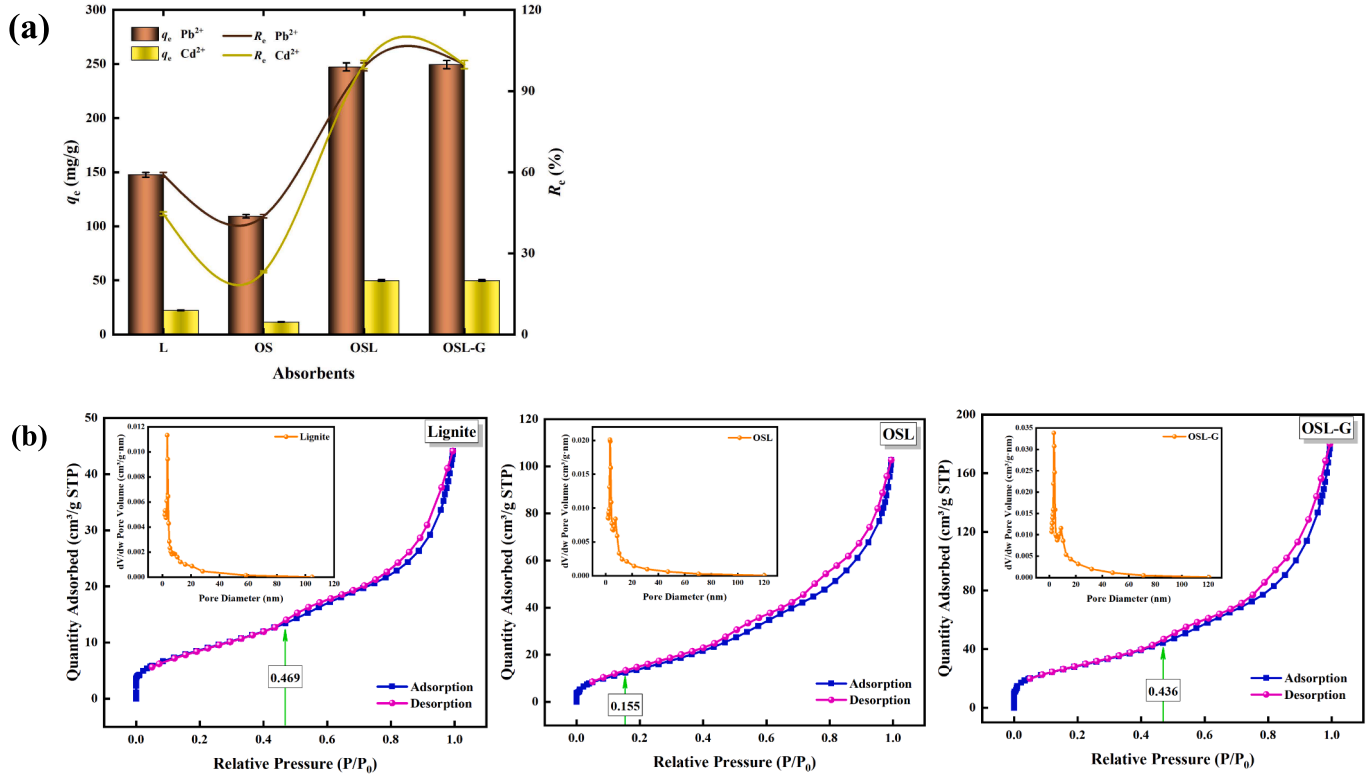

Fig. 3. (a) Removal rates of Pb^{2+} and Cd^{2+} by lignite, oyster shells, OSL, and OSL-G. (the OSL-G dosage is 4 g/L, others dosage are all 0.2 g/L, pH = 4, C_0 (Pb^{2+}) is 50 mg/L, C_0 (Cd^{2+}) is10mg/L, the temperature is 25 °C, reaction time is 24 h). (b) N_2 adsorption–desorption isothermal curves and pore size distribution curves of lignite, OSL, and OSL-G.

lignite and 2.26 times (Pb^{2+}) and 4.31 times (Cd^{2+}) for single oyster shell, respectively. The removal rates of Pb^{2+} and Cd^{2+} by OSL-G were 99.78 % and 99.77 %, respectively, and the adsorption capacity of Pb^{2+} and Cd^{2+} were 12.47 mg/g, 2.49 mg/g, respectively. It significantly improved the removal rate compared with that of single lignite or oyster shell materials, respectively, by 1.69 (Pb^{2+}) times and 2.23 (Cd^{2+}) times for single lignite and 2.28 times (Pb^{2+}) and 4.31 times (Cd^{2+}) for single oyster shells.

The BET analysis results of lignite, OSL, and OSL-G are shown in Fig. 3(b). It can be seen from Fig. 3(b), that the N_2 adsorption–desorption isotherms of lignite, OSL, and OSL-G were typical type II isotherms, indicating that mesoporous or mesoporous (2 ~ 50 nm) dominant for both adsorbents (Samanta et al., 2016a; Samanta et al., 2016b). The adsorption–desorption curves of the three adsorbents at the low pressure almost completely coincided and showed a partial Y-axis, which indicated that the pore size of the three adsorbents was more uniform, the pore arrangement was more ordered, and the three adsorbents had a strong force with nitrogen. lignite, OSL, and OSL-G began to bifurcate when the relative pressure was 0.469, 0.155, and 0.436, respectively, and the adsorption–desorption curves did not overlap to produce a hysteresis loop, which may be because the material began to condense and accumulate capillary pores. The isotherms of three adsorbents conformed to the typical H3-type lag loop (Samanta et al., 2017), indicating that lignite, OSL, and OSL-G were dominated by slit pores formed by the accumulation of sheet particles. Lignite, OSL, and OSL-G contained a large number of mesoporous structures, and the pore sizes were mainly concentrated in the range of 3 ~ 10 nm.

The pore structure parameters of lignite, OSL, and OSL-G composites are shown in Table 2. It can be seen from Table 2 that the surface area, pore size, and pore volume characteristics of lignite have changed after modification. The order of specific surface area (S_{BET}) and total pore volume (V_{tot}) of the three adsorbents was OSL-G > OSL > Lignite, which indicated that the composites prepared by the two methods have larger specific surface area and porosity than lignite, especially OSL-G. The pore size of the three adsorbents was OSL-G > Lignite > OSL, which indicated that OSL had a more microporous structure than lignite, while OSL-G had more mesoporous or macroporous structure than lignite.

Table 2
Specific surface area, total pore volume and pore diameter parameters of lignite, OSL and OSL-G.

Parameters	lignite	OSL	OSL-G
Specific surface area (m^2/g)	32.0523	55.0809	103.9347
Total pore volume (cm^3/g)	0.0667	0.1549	0.2765
Pore diameter (nm)	8.0304	7.8464	8.3334

3.3. Adsorption properties

3.3.1. Effect of adsorbent dosage

In Fig. 4(a), it is evident that when the adsorbent dosage is between 1 and 2 g/L, the OSL-G adsorption site can be fully utilized, resulting in an increase in the removal rate of Pb^{2+} from 48.48 % to 98.12 %. Further increasing the dosage has minimal impact on the removal rate of Pb^{2+}. Thus, the optimal dosage for OSL-G adsorbing Pb^{2+} is considered to be 2 g/L. For the adsorption of Cd^{2+}, increasing the dosage of OSL-G from 1 g/L to 4 g/L leads to an increase in the removal rate of Cd^{2+} from 30.21 % to 99.45 %. Continuing to increase the dosage has little significance, indicating that the optimal dosage for OSL-G adsorbing Cd^{2+} is considered to be 4 g/L. The improvement in adsorption can be attributed to the increase in surface area and the availability of more adsorption-binding sites (Pérez et al., 2022; Zhang et al., 2019). The difference in dosage required for the effective removal of Pb^{2+} and Cd^{2+} by OSL-G is related to their difference in radius, hydration energy, and solubility product constant. Compared with Cd^{2+}, Pb^{2+} has a smaller radius, lower hydration energy, smaller solubility product constant, and is more prone

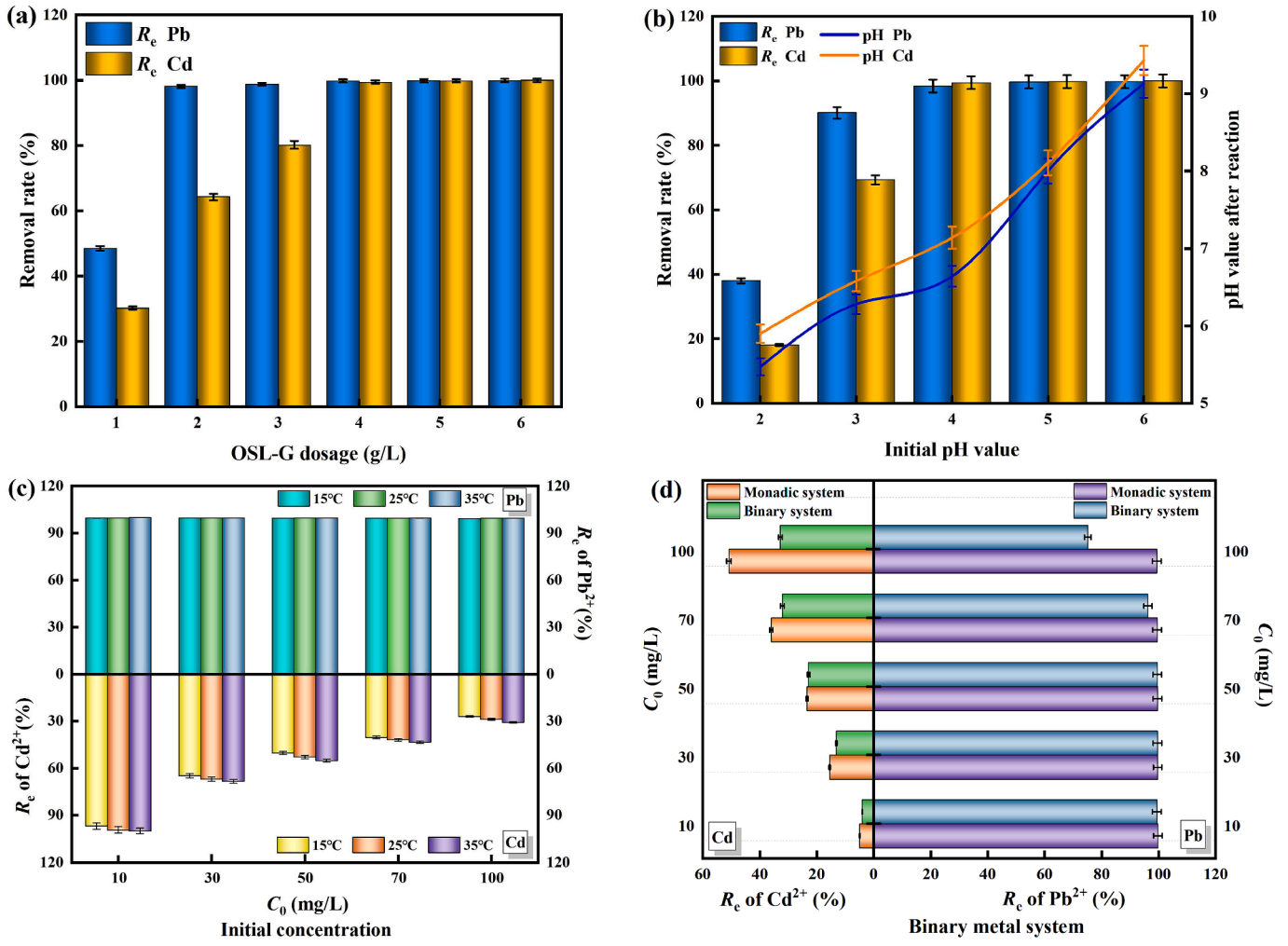

Fig. 4. Effect of the adsorbent dosage (a), initial pH value (b), initial concentration (c), binary metal system (d) on the adsorption of Pb^{2+} and Cd^{2+} by OSL-G.

to precipitation, ion exchange, and complexation reactions. Therefore, the optimal dosage for the adsorption of Pb^{2+} by OSL-G is only 2 g/L, while the optimal dosage for the adsorption of Cd^{2+} is up to 4 g/L.

3.3.2. *Effect of initial pH*

It can be seen from Fig. 4(b), with the initial pH value increasing from 2 to 4, the removal rate of Pb^{2+} by OSL-G significantly increased from 38 % to 98.39 %, and the removal rate of Cd^{2+} increased from 18.06 % to 99.45 %. A similar behavior was found by Du et al. (2011) using two types of mollusk shell powders to remove Pb^{2+}, Cd^{2+} and Zn^{2+}. As the initial pH continued to increase from 4 to 6, the removal rate of Pb^{2+} and Cd^{2+} by OSL-G increased slightly and tended to be stable. The initial pH of the solution system will affect the electrostatic interaction, surface precipitation, and adsorption reaction between the two (Liu et al., 2009). The increase of initial pH and the low concentration of H^+ is conducive to reducing the competition between H^+, Pb^{2+}, and Cd^{2+}, leaving more adsorption sites remaining on the surface of OSL-G and removal of target pollutants. The high concentration of OH^- in the solution will increase the negative charge on the surface of OSL-G, thereby reducing the electrostatic repulsion of OSL-G with Pb^{2+} and Cd^{2+}. It is also conducive to the neutralization and precipitation or the existence form of multiple basic ions.

It can be seen from Fig. 4(b) that the initial pH value is in the range of 2 ~ 5, and the pH of the solution system after the reaction is all within 9. The pH range of AMD that OSL-G can handle is more extensive. In addition, pH affects the reaction mechanism of removing Pb^{2+} and Cd^{2+}, and the stability of compounds generated by different reaction mechanisms is different (Pehlivan et al., 2008; Li et al., 2017). When pH < 7, Pb^{2+} and Cd^{2+} exist as ions, and the removal of metal ions by the composite is mainly based on ion exchange and surface complexation. When the pH of the solution is between 7 and 9, Pb^{2+} and Cd^{2+} mainly exist in the form of $Pb(OH)^+$, $Cd(OH)^+$, $Pb(OH)_2$, and $Cd(OH)_2$, and the metal removal of the composite is mainly precipitated. When the solution pH > 9, Pb^{2+} and Cd^{2+} mainly exist in the form of $Pb(OH)_2$, $Pb(OH)_3^-$, $Pb(OH)_4^{2-}$, $Cd(OH)_2$, $Cd(OH)_3^-$ (Kolodynska et al., 2012; Jiang et al., 2020). The removal of metals by composite materials is mainly caused by precipitation, but the high pH value will lead to the secondary dissolution of hydroxide precipitation (Frišták et al., 2015). Therefore, considering the adsorption effect and the product stability of the adsorption reaction, it is considered that the initial pH value of 4 is more advantageous.

3.3.3. *Effect of initial concentrations of Pb^{2+} and Cd^{2+}*

It can be seen from Fig. 4(c), that in the same temperature system, as the initial concentrations of Pb^{2+} and Cd^{2+} increase, the removal rates of Pb^{2+} and Cd^{2+} by OSL-G gradually decrease. This is because at a low initial concentration, compared with the amount of Pb^{2+} and Cd^{2+} in the solution, the number of effective adsorption sites on the surface of OSL-G is quite sufficient, which is conducive to the diffusion of Pb^{2+} and Cd^{2+} to the adsorption site and binding with it to promote the adsorption reaction (Jamshidifard et al., 2019). The concentration difference between the solution and the surface of the composite material increases, which strongly drives the Pb^{2+} and Cd^{2+} in the solution to move rapidly to the OSL-G surface, increasing the chance of interaction between Pb^{2+}

and Cd^{2+} and the active site (Awang et al., 2019; Liu et al., 2020). However, with the advancement of the reaction process, the fewer the remaining adsorption sites, the adsorption gradually reaches saturation, and after the adsorption of Pb^{2+} and Cd^{2+}, the surface of the composite material will accumulate excessive positive charges, which is difficult to continue adsorption with more free metal ions in the solution, so the removal rate is gradually reduced. At the same concentration level, the removal rates of Pb^{2+} and Cd^{2+} by OSL-G increased with the rise in ambient temperature, suggesting that the adsorption process of Pb^{2+} and Cd^{2+} by OSL-G is endothermic. As the temperature increases, the proportion of activated ions in the solution also increases. This leads to a faster diffusion rate of Pb^{2+} and Cd^{2+} towards the surface of the composite material. Consequently, there is a higher likelihood of effective collision with the functional groups on the surface of the composite material, resulting in an increased level of adsorption equilibrium. Similar results have also been described in previous articles (Ogata et al., 2018; Arslanoglu et al., 2019; Cherdchoo et al., 2019).

According to the "Comprehensive Sewage Discharge Standard" (GB 8978–1996), the maximum allowable emission limits for Pb^{2+} and Cd^{2+} are 1 mg/L and 0.1 mg/L, respectively. In this experiment, the initial concentrations of Pb^{2+} and Cd^{2+} in simulated AMD were 50 mg/L and 10 mg/L, respectively. To meet the AMD emission standard after treatment, the removal rates of Pb^{2+} and Cd^{2+} should reach 98 % and 99 %, respectively. Comparing the removal rates of Pb^{2+} and Cd^{2+} by OSL-G at different initial concentrations and temperatures, it was found that the removal rates of Pb^{2+} can exceed 99 % when the initial concentration is between 10 and 100 mg/L. However, when the initial concentration of Cd^{2+} increased from 10 mg/L to 30 mg/L, the removal rate dropped significantly from more than 99 % to less than 70 %. In summary, 2 g/L OPL-G can treat AMD with an initial concentration of Pb^{2+} ranging from 10 to 100 mg/L, and 4 g/L OPL-G can treat AMD with an initial concentration of Cd^{2+} ranging from 0 to 10 mg/L. Since the content of Cd in acid mine wastewater is generally low and the content of Pb is high, the treatment of Pb and Cd pollution in AMD by OSL-G has certain advantages.

3.3.4. *Effect of the binary metal system*

In Fig. 4(d), it is evident that the adsorption effect of OSL-G on Pb^{2+} and Cd^{2+} in the binary metal system is lower than that in the monadic metal system, and the higher the initial concentration is, the more significant the competitive effect of Pb^{2+} and Cd^{2+} is. This is because in the binary system, the total amount of metal ions in the solution is higher than that in the monadic metal system, and the points that can be provided by adding the same amount of materials are limited, resulting in competition between ions (Huang et al., 2020; Zaman et al., 2023). On the whole, the removal rate of Pb^{2+} is higher than that of Cd^{2+}, indicating that OSL-G has a higher selectivity and better removal effect on Pb^{2+} in a non-equal competition system. The selective adsorption of heavy metal ions depends on the physical and chemical properties of metal ions (hydrolysis constant, radius of hydrated ion, molar mass, and solubility product constant of metal ion hydroxide). The smaller the hydrolysis constant of metal ions is, the easier the ions are to be adsorbed. The hydrolysis constant of Pb^{2+} (7.8) is significantly lower than that of Cd^{2+} (9.2). For homogeneous metal cations, the smaller the hydration radius, the easier it is to diffuse through the boundary layer to the surface of the adsorbed material. The hydration radius of Pb^{2+} (0.401 mm) is smaller than that of Cd^{2+} (0.426 mm), the mass transfer resistance of Pb^{2+} in solution is smaller, and the ion exchange reaction is more likely to occur. The higher the molar mass of metal ions, the more likely a precipitation reaction occurs. The molar mass of Pb^{2+} (207.2 g/mol) is almost twice that of Cd^{2+} (112.4 g/mol), and the adsorption preference of Pb^{2+} is stronger. The lower the solubility of hydroxide of the same valent metal ion, the easier it is to react with OH^- to form chemical precipitation. The hydroxide solubility product constant of Pb^{2+} (1.2×10^{-15}) is smaller than that of Cd^{2+} (2.2×10^{-14}). Therefore, it can be concluded that the selection order of Pb^{2+} and Cd^{2+} by OSL-G is $Pb^{2+} > Cd^{2+}$, which is also verified by similar research results (Wan et al., 2014; Bohli et al., 2015; Gameli et al., 2023).

It can also be seen from Fig. 4(d) that in the Pb-Cd binary metal system (Cd^{2+}=10 mg/L, Pb^{2+} = 10–100 mg /L), the removal effect of OSL-G on Pb^{2+} remains almost unchanged, both remaining above 99 %. In the Cd-Pb binary metal system (Pb^{2+} = 10 mg/L, Cd^{2+} = 10 mg/L), the effect of Pb^{2+} competitive adsorption on the removal of Cd^{2+} by OSL-G adsorption is also low, and the removal rate of Cd^{2+} can be ensured above 99 %. Therefore, adding 4 g/L OSL-G to treat the simulated AMD-containing binary metal system (pH = 4, Pb^{2+} = 10 mg/L, Cd^{2+} = 10 mg/L) can effectively remove 99.38 % of Pb^{2+} and 99.02 % of Cd^{2+}, and the pH of the solution system after reaction is around 7. The effluent water quality conforms to the "Comprehensive Sewage Discharge Standard" (GB 8978-1996).

3.4. *Adsorption kinetics, isotherm, thermodynamics*

3.4.1. *Adsorption kinetics*

The adsorption process can generally be described as three processes: the diffusion on the surface of the adsorbent, the diffusion in the adsorbent particles, and the adsorption on the porous adsorption site. The time consumed at each stage affects the rate of the entire adsorption process (Li et al., 2019). Quasi-first-order kinetic and quasi-second-order kinetic adsorption models (Fig. 5(a and b)) and inter-particle diffusion models (Fig. 5(c and d)) were used to fit the adsorption processes of Pb^{2+} and Cd^{2+} by OSL-G, determine the adsorption rate control steps and explore the adsorption mechanism. The adsorption parameters of the kinetic models are shown in Table 3.

It can be seen from Fig. 5(a and b) that, compared with the quasi-first-order kinetic model, the R^2 of the quasi-second-order kinetic model is closer to 1, and the theoretically calculated value of the adsorption capacity of Pb^{2+} and Cd^{2+} by OSL-G obtained by this model is closer to the actual experimental value. The parameter results in Table 3 show that the quasi-second-order kinetic model can more accurately reflect the adsorption process. The establishment theory of the quasi-second-order kinetic model assumes that the adsorption rate is controlled by the chemisorption mechanism and is determined by the square of the number of remaining adsorption vacancies on the surface. Therefore, it can be considered that the adsorption rate is directly proportional to the quadratic of the driving force. In addition, during the adsorption process, Pb^{2+} and Cd^{2+} will react with the internal substances of OSL-G particles to form new chemical bonds, which will transform them into new substances and remove them, and their adsorption rate is mainly controlled by chemisorption. It can be seen from Fig. 5(c and d), there are three stages in the adsorption process of Pb^{2+} and Cd^{2+} by OSL-G. The first stage is the rapid diffusion of Pb^{2+} and Cd^{2+} through the boundary film to the surface of OSL-G, which is reflected as surface diffusion. The second stage is the slow diffusion of Pb^{2+} and Cd^{2+} to the mesopore in OSL-G, and the third stage is mainly the micropore diffusion, and the adsorption process is slow until the adsorption equilibrium is reached (Liang et al., 2018). The fitting parameters in Table 3 show that the order of diffusion rates of Pb^{2+} and Cd^{2+} is $K_{31} > K_{32} > K_{33}$, and the order of boundary layer thickness is $C_1 < C_2 < C_3$, which indicates that the boundary layer thickened continuously with the advancement of the adsorption process of Pb^{2+} and Cd^{2+} by OSL-G. The thickening of the boundary layer obstructs the diffusion, leading to the deviation of the adsorption process from the internal diffusion model. The fitted curves do not pass through the origin, and the deviation degree is increasing, which also verifies the above analysis results. The deviation of the inter-particle diffusion model from the origin indicates that the adsorption process is controlled by the external and internal diffusion of the particles (Wang et al., 2019). The low R^2 of the fitted inter-particle diffusion model also indicates that the entire adsorption process is mainly dominated by chemical adsorption.

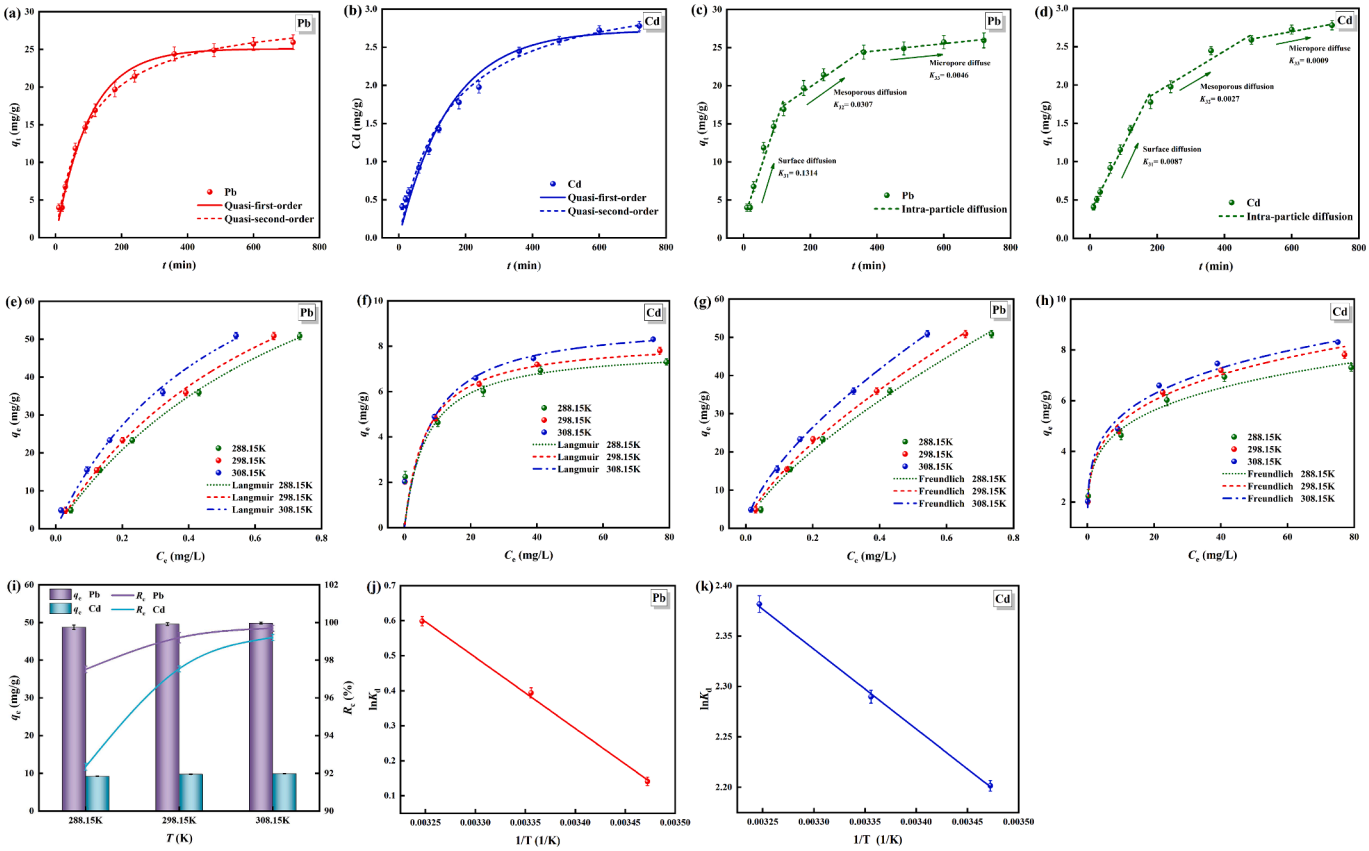

Fig. 5. Adsorption kinetics, isotherms, thermodynamics of Pb^{2+} and Cd^{2+} by OSL-G. (a) Adsorption kinetics of Pb^{2+}, (b) Adsorption kinetics of Cd^{2+}, (c) Intra-particle diffusion model of Pb^{2+}, (d) Intra-particle diffusion model of Cd^{2+}, (e) Langmuir model of Pb^{2+}, (f) Langmuir model of Cd^{2+}, (g) Freundlich model of Pb^{2+}, (h) Freundlich model of Cd^{2+}, (i) Effect of temperature on the adsorption of Pb^{2+} and Cd^{2+} by OSL-G, (j) Adsorption thermodynamics of Pb^{2+}, (k) Adsorption thermodynamics of Cd^{2+}.

Table 3
Adsorption kinetic parameters for adsorption of Pb^{2+} and Cd^{2+} by OSL-G.

Model	Pb^{2+}	Cd^{2+}
Quasi-first-order		
K_1 (/min)	0.0098	0.0065
q_e (mg/g)	25.0791	2.7254
R^2	0.9876	0.9767
Quasi-second-order		
K_2 (g/(mg·min))	0.00034	0.0020
q_e (mg/g)	30.0523	3.3659
R^2	0.9918	0.9859
Intra-particle diffusion		
K_{31}(mg/(g·min$^{1/2}$))	0.1314	0.0087
C_1	2.4313	0.3442
R_1^2	0.9554	0.9901
K_{32}(mg/(g·min$^{1/2}$))	0.0307	0.0027
C_2	13.7095	1.3782
R_2^2	0.9645	0.8795
K_{33}(mg/(g·min$^{1/2}$))	0.0046	0.0009
C_3	22.7539	2.2099
R_3^2	0.9332	0.8968

3.4.2. Adsorption isotherm

The adsorption isotherm can effectively determine the distribution of adsorbents in the solid–liquid phase, which is of great significance for evaluating the adsorption process of Pb^{2+} and Cd^{2+} by OSL-G (El Atouani et al., 2019). The Langmuir adsorption isotherm model (Fig. 5(e and f)) and Freundlich adsorption isotherm model (Fig. 5(g and h)) were used to fit the adsorption processes of Pb^{2+} and Cd^{2+} by OSL-G. The fitting parameters of the isotherm model are shown in Table 4. As shown in Fig. 5(e–h) and Table 4, R2 of the Langmuir model is smaller than that of the Freundlich model at 288.15 K, 298.15 K, and 308.15 K temperatures. It can be seen that the adsorption of Pb^{2+} and Cd^{2+} by OSL-G at different temperatures is more suitable to be explained by the Freundlich adsorption isothermal model, indicating that the adsorption process is multi-layer non-uniform adsorption (Homagai et al., 2022). The K_F values of Pb^{2+} and Cd^{2+} adsorbed by OSL-G increased slightly with increasing temperature, indicating that the affinity of OSL-G to Pb^{2+} and Cd^{2+} was improved by increasing temperature. n reflects the strength of adsorption, and $1/n$ is the concentration index commonly used to evaluate adsorption. The smaller the value, the better. The $1/n$ values are all between 0 and 1, indicating that the adsorption reaction is easy to carry out (Kim and Singh, 2022).

The adsorption capacity of OSL-G and OSL for Pb^{2+} and Cd^{2+} in aqueous media was compared with that of other adsorbent materials (Table 5). It can be seen from Table 5, the maximum adsorption capacity of OSL-G for Pb^{2+} and Cd^{2+} was in the middle level, especially the adsorption capacity of Cd^{2+} was not high. Through further analysis of this phenomenon, it was found that the adsorption time, temperature, and adsorbent morphology were the key factors affected the adsorption capacity, especially the adsorbent morphology. Other materials with high adsorption capacity in Table 5 were powdery with small particle size, while OSL-G was granular, which also become an important reason for the low adsorption capacity of OSL-G. Therefore, based on the importance of adsorbent morphology, the adsorption capacity of powdered OSL was investigated, and it was found that the adsorption capacity was greatly improved, which was sufficient to prove the excellent performance of the adsorption material. Interestingly,

Table 4
Adsorption isotherm constants for adsorption of of Pb^{2+} and Cd^{2+} by OSL-G.

Model	Pb^{2+}			Cd^{2+}		
	288.15 K	298.15 K	308.15 K	288.15 K	298.15 K	308.15 K
Langmuir						
K_L	1.1634	1.3492	1.8743	0.1316	0.1485	0.1871
Q_m (mg/g)	109.7384	107.2821	99.5546	7.6275	8.3777	9.0206
R^2	0.9953	0.9975	0.9940	0.7748	0.8370	0.8429
R_L	0.0085 ~ 0.0791	0.0074 ~ 0.0690	0.0053 ~ 0.0507	0.07063 ~ 0.4318	0.0631 ~ 0.4025	0.0507 ~ 0.3483
Freundlich						
K_F	64.1794	68.6982	76.3436	2.9993	3.1048	3.3237
$1/n$	0.7135	0.6979	0.6617	0.2117	0.2182	0.2141
R^2	0.9980	0.9983	0.9997	0.9837	0.9896	0.9879

Table 5
Comparison of the maximum adsorption capacity of Pb^{2+} and Cd^{2+} with other adsorbents.

Adsorbent	adsorbate	temperature	time	adsorption capacity (mg/g)	BET surface area (m^2/g)	Reference
$KMnO_4$-treated magnetic biochar (FMBC)	Pb^{2+}	25 °C	24 h	148	137	Sun et al., 2019
	Cd^{2+}			79		
CA-enriched biochar of Chickpea	Pb^{2+}	25 °C	24 h	12.1094	—	Nazari et al., 2019
	Cd^{2+}			2.4757		
Cassava root husk-derived biochar with ZnO nanoparticles (CRHB-ZnO3)	Pb^{2+}	25 °C	60 min	44.27	2.7964	Tho et al., 2021
	Cd^{2+}			42.05		
Amine-functionalized magnesium ferrite-biochar composite ($MgFe_2O_4$–NH_2@sRHB)	Pb^{2+}	25 °C	24 h	198.93	51.30	Li et al., 2022
	Cd^{2+}			195.50		
Fe/S functionalized biochar (BC-Fe-S)	Pb^{2+}	45 °C	120	124.62	41.30	Cao et al., 2022
	Cd^{2+}		min	57.71		
Mg/Fe bimetallic oxide-modified biochar	Pb^{2+}	25 °C	480	283.4	332.84	Cheng et al., 2023
	Cd^{2+}		min	195.5		
oyster shell loaded lignite composite adsorbent in powdery morphology (OSL-G)	Pb^{2+}	25 °C	720	107.2821	103.9347	This work
	Cd^{2+}		min	8.3777		
oyster shell loaded lignite composite adsorbent in powdery morphology (OSL)	Pb^{2+}	25 °C	720	332.62	102.676	
	Cd^{2+}		min	318.98		

although the powder adsorption effect is good, but compared with the powder adsorbent, the granular adsorbent has the advantage of easy solid–liquid separation and sedimentation. The effect of different morphologies of adsorbents on pollutants in water has also become an important direction of follow-up research.

3.4.3. Adsorption thermodynamics

The temperature has a certain effect on the adsorption reaction. It is necessary to explore the thermodynamic changes in the adsorption process of OSL-G to determine the spontaneity of the adsorption of Pb^{2+} and Cd^{2+}. The adsorption experiments were carried out at three temperature conditions of 288.15 K, 298.15 K, and 308.15 K, respectively (Fig. 5(i)), and thermodynamic adsorption curves were drawn with $\ln K_d$ as Y-axis and $1/T$ as X-axis (Fig. 5(j and k)). The thermodynamic parameters of the adsorption process are shown in Table 6. It can be seen from Fig. 5(i–k), that the removal efficiency of Pb^{2+} and Cd^{2+} showed an increasing trend with the increase of temperature. In Table 6, the Gibbs free energy ΔG is negative at all temperatures, indicating that the adsorption of Pb^{2+} and Cd^{2+} by OSL-G is spontaneous (Sun et al., 2015). The higher the temperature, the smaller the ΔG, and the more likely the spontaneous reaction is to occur. The enthalpy change ΔH is positive, which also proves that the adsorption reaction is an endothermic process. The entropy change ΔS is positive, indicating that the adsorption process is a process of entropy increase, which means that the adsorption process of Pb^{2+} and Cd^{2+} is inevitably accompanied by the desorption of other ions at the adsorption site on the surface of OSL-G, which increases the chaos and disorder of the whole system during the adsorption process (Lin et al., 2018).

Table 6
Thermodynamic parameters for adsorption of Pb^{2+} and Cd^{2+} by OSL-G.

Pollutants	ΔG (kJ/mol)			ΔH(kJ/mol)	ΔS(J/(mol·K))
	288.15 K	298.15 K	308.15 K		
Pb^{2+}	−0.3386	−0.9769	−1.5326	16.8914	59.8599
Cd^{2+}	−5.2714	−5.6734	−6.0988	6.6392	41.3436

3.5. Microscopic characterization and adsorption mechanism

3.5.1. SEM

It can be seen from Fig. 6(a), that the surface of lignite is relatively smooth and dense, but there are also some micropores and lamellar accumulations on the surface, with some folds and voids (Zhang and Chen, 2020; Jellali et al., 2021). There are many cracks, pores, and scaly structures on the surface of OSL-G, and a large number of fine particles, flake structures, and massive structures accumulate. High-temperature roasting results in the release of water and some organic matter in lignite, the pore structure shrinks and collapses, and the surface roughness increases (He et al., 2019). The scale structure of the bentonite binder is retained, which makes the structure of OSL-G loose and porous. Oyster shells decompose into CaO and CO_2 when roasted. This analysis is also supported by the significant reduction of the content of C and O in OSL-G compared with that in lignite. A large amount of CO_2 escape will play a role in opening pores and increasing the number of pores in OSL-G. At the same time, the CaO generated by roasting at high temperatures will enter the bentonite and lignite layers and combine with SiO_2, silicate precursors or alumino-silicate precursors to form C-S-H, C-A-H, C-A-S-H and other crystals or amorphous gels, which are deposited in the form of fine particles, flake structure or block structure to increase the surface area of the material (Wang et al., 2011; Li et al., 2012; Hao et al., 2019). After adsorption of Pb^{2+} and Cd^{2+}, OSL-G (Pb^{2+}) and OSL-G (Cd^{2+}) are attached to a large number of substances

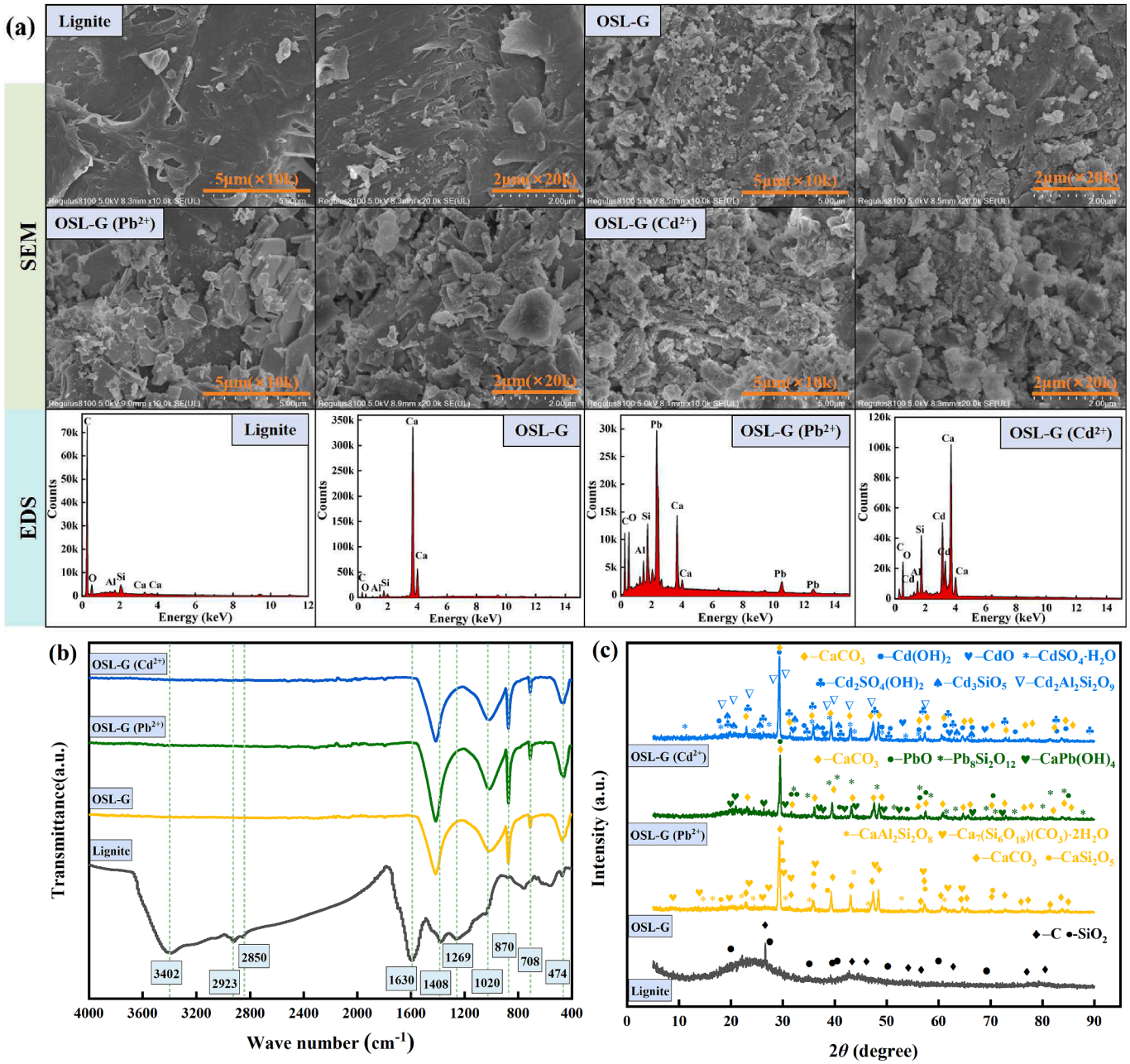

Fig. 6. Microscopic characterization results of Pb^{2+} and Cd^{2+} adsorbed by OSL-G. (a) SEM-EDS, (b) FTIR, (c) XRD.

with different forms, and the aggregation state increases. Compared with the EDS diagram, it can be seen that there are no Pb and Cd elements in OSL-G, while Pb and Cd elements appear in OSL-G (Pb^{2+}) and OSL-G (Cd^{2+}), which indicates that the adsorption sites of OSL-G successfully interact with Pb^{2+} and Cd^{2+}, and the products adhere stably to their surfaces.

3.5.2. FTIR

It can be seen from Fig. 6(b), in the peak spectrum of lignite, the –OH stretching vibration absorption peak corresponding to 3402 cm^{-1} and the –OH bending vibration absorption peak corresponding to 1630 cm^{-1} both weaken after granulation, which can be attributed to the loss of water in lignite during roasting (Zhang et al., 2016). The absorption peaks at 1269, 2923, and 2850 cm^{-1} were derived from the residue of organic matter in lignite material, and the peaks disappeared in the OSL-G peak spectrum after roasting. In the OSL peak spectrum, the in-plane and out-plane deformation vibrations of C-O and the stretching and bending vibrations of Ca-O appear near 708, 870, and 1408 cm^{-1}, indicating the presence of Ca-O and CO_3^{2-} in OSL-G (Feng et al., 2022). By comparing the peak spectra of lignite and OSL-G, it is found that there are Si-O-Si characteristic absorption peaks near 474 and 1020 cm^{-1}, and OSL-G is significantly enhanced compared with the Si-O-Si characteristic absorption peaks in lignite, which means that a new silicate or silicon oxide appears in OSL-G. By comparing the peak spectra before and after adsorption of Pb^{2+} and Cd^{2+}, it is found that the absorption peaks near 474 and 1020 cm^{-1} are enhanced in different amplitude, indicating that Si-O-Si participated in the adsorption reaction process. In addition, the absorption peaks of 708, 870, and 1408 cm^{-1} still existed, indicating that the adsorption did not destroy the structure of OSL-G, but the intensity of the absorption peak increased to different degrees, indicating that Ca-O and C-O participated in the adsorption of Pb^{2+} and Cd^{2+}.

3.5.3. XRD

It can be seen from Fig. 6(c), that lignite is mainly composed of organic carbon molecules and inorganic minerals. Lignite has an obvious characteristic peak at $2\theta = 26.603°$, which is the (0 0 3) plane diffraction peak of carbon. This proves that lignite is an amorphous carbon structure (He et al., 2019). The (1 0 0) plane diffraction peaks of SiO2 appear at $2\theta = 20.859°$ and 26.639°, indicating that the minerals of lignite are composed of quartz (Abdelsayed et al., 2018). The EDS results showed that lignite still contained a certain amount of Al element, but no aluminum compounds were found in the phase detection because of its low content and small crystal structure. The characteristic peak of SiO_2 in OSL-G disappeared because part of SiO_2 participated in the reaction to produce $CaCO_3$, $CaSi_2O_5$, $CaAl_2Si_2O_8$, and $Ca_7(Si_6O_{18})(CO_3)\cdot 2H_2O$ mineral phases, and the other part of SiO_2 became an amorphous gel. $CaCO_3$ is the main component of calcite in oyster shells. During the sintering process at 640 °C, the middle part of $CaCO_3$ will decompose into CaO. Part of CaO will react with SiO_2, the main component of lignite, to form $CaSi_2O_5$, while the other part of CaO will undergo a hydrolysis reaction with surrounding water and be transformed into Ca $(OH)_2$. $Ca(OH)_2$ will continue to react with SiO_2, aluminum-containing oxides, and other volcanic ash to form $CaAl_2Si_2O_8$ and $Ca_7(Si_6O_{18})(CO_3)\cdot 2H_2O$.

The main mineral phases of OSL-G (Pb^{2+}) are $CaCO_3$, PbO, $Pb_8Si_2O_{12}$, and $CaPb(OH)_4$. Compared with OSL-G before adsorption, $CaCO_3$ still exists after the reaction, and a new mineral phase appears during the adsorption of Pb^{2+}. The new product PbO after the reaction is caused by the precipitation of $Pb(OH)_2$ generated by the reaction of Pb^{2+} and OH^- during the collection and drying process. $Pb_8Si_2O_{12}$ is thought to be produced by ion exchange reaction between Pb^{2+} and silicates in OSL-G or electrostatic adsorption with free silicates in solution. CaPb $(OH)_4$ is the product of synergistic precipitation of Ca^{2+}, Pb^{2+}, and OH^-. After OSL-G adsorbed Cd^{2+}, $CaCO_3$ still existed, and new mineral phases including $Cd(OH)_2$, CdO, $CdSO_4\cdot H_2O$, $Cd_2SO_4(OH)_2$, Cd_3SiO_5, $Cd_2Al_2Si_2O_9$ were generated. The $Cd(OH)_2$ generated after the reaction is the product of the precipitation reaction between Cd^{2+} and OH^-, and the CdO is the product of the thermal decomposition of $Cd(OH)_2$, which indicates that OSL-G can release a certain amount of OH^-. $CdSO_4\cdot H_2O$ is formed after the reaction, which is caused by an ion exchange reaction between Cd^{2+} and metal sulfate existing in lignite, and a complex reaction between Cd^{2+}, OH^- and SO_4^{2-}. The reasons for the generation of $Cd_2SO_4(OH)_2$ are relatively complex, partly due to the complexation of Cd^{2+}, OH^- and SO_4^{2-}, and partly due to the precipitation and accumulation of $Cd(OH)_2$ generated by the adsorption and precipitation of OSL-G with dissolved Cd^{2+} in solution, resulting in a large number of new pores. And then continue to adsorb Cd^{2+}, SO_4^{2-}, OH^- produced by the water. Cd_3SiO_5 is thought to be the result of ion exchange between Cd^{2+} and silicates in OSL-G or electrostatic adsorption with silicates in solution. The mineral phase of $Cd_2Al_2Si_2O_9$ is formed by the reaction of Cd^{2+}, Al^{3+}, and silicate ions. Similar results were obtained in the studies of Bartczak et al. (2018), Hao et al. (2019) and Wang et al. (2022).

In conclusion, there are four potential mechanisms for the adsorption of Pb^{2+} and Cd^{2+} by OSL-G (Fig. 7). i, electrostatic adsorption. ii, Pb^{2+} and Cd^{2+} generate metal oxide precipitates on their surfaces. iii, the ion exchange between Pb^{2+} and Cd^{2+} and their surface Ca^{2+}. iiii, the surface complexation mechanism of Pb^{2+} and Cd^{2+} with their surface oxygen-containing functional groups.

3.6. Regeneration and utilization

The desorption rates of Pb^{2+} and Cd^{2+} for different desorption solutions are shown in Fig. 8(a). It can be seen from Fig. 8(a) that acidic and alkaline solutions have better desorption effects on Pb^{2+} and Cd^{2+}, and the desorption rate is the lowest in the H_2O solution. When the desorption solution is 1 mol/L HNO_3, the desorption rates of Pb^{2+} and Cd^{2+} are 74.65 % and 70.52 %, respectively. This may be because when the solution is acidic, there is more H^+ in the solution, and H^+ can compete with the adsorption sites of Pb^{2+} and Cd^{2+} for ROSL-G. When the desorption solution is 1 mol/L NaOH, the desorption rates of Pb^{2+} and Cd^{2+} are the highest, which are 89.06 % and 85.45 % respectively. Because in the alkaline environment, OH^- in the solution can form Pb

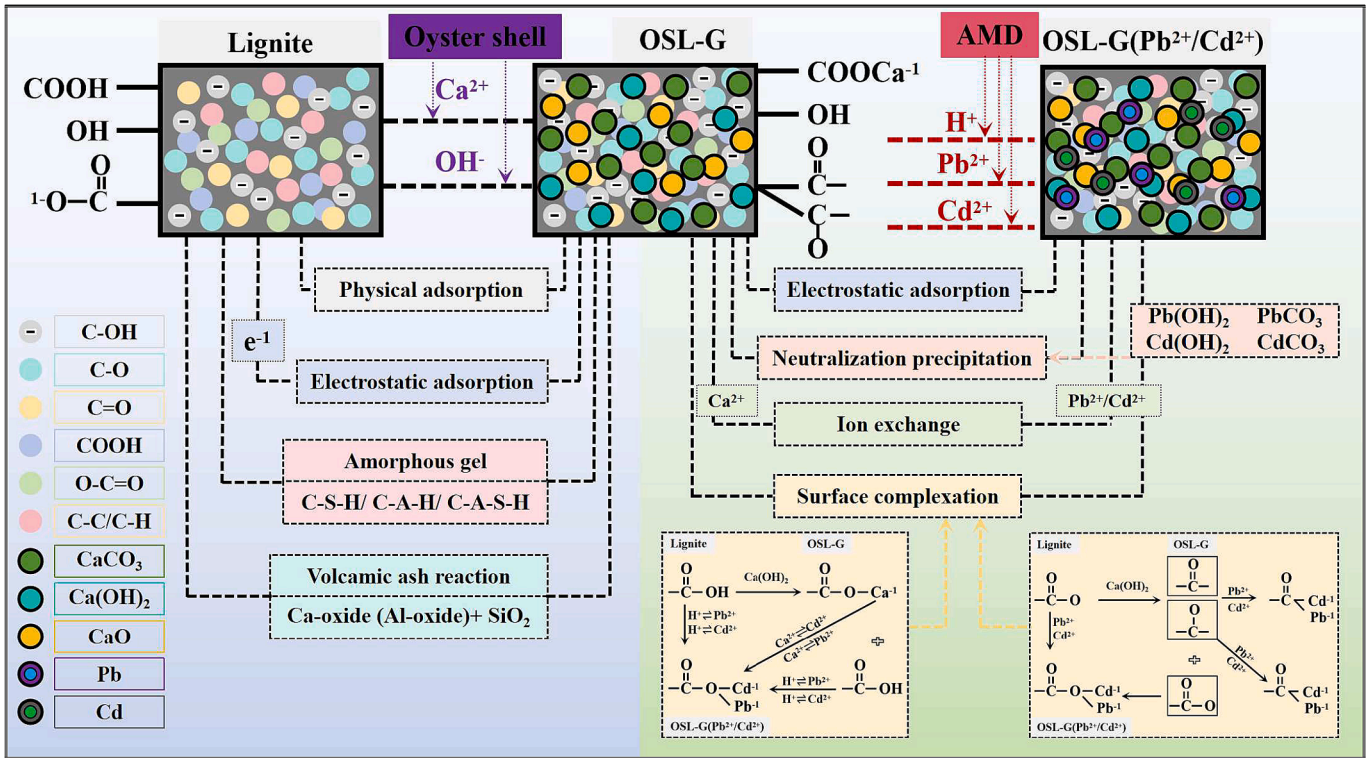

Fig. 7. The potential mechanism of the adsorption for Pb^{2+} and Cd^{2+} by OSL-G.

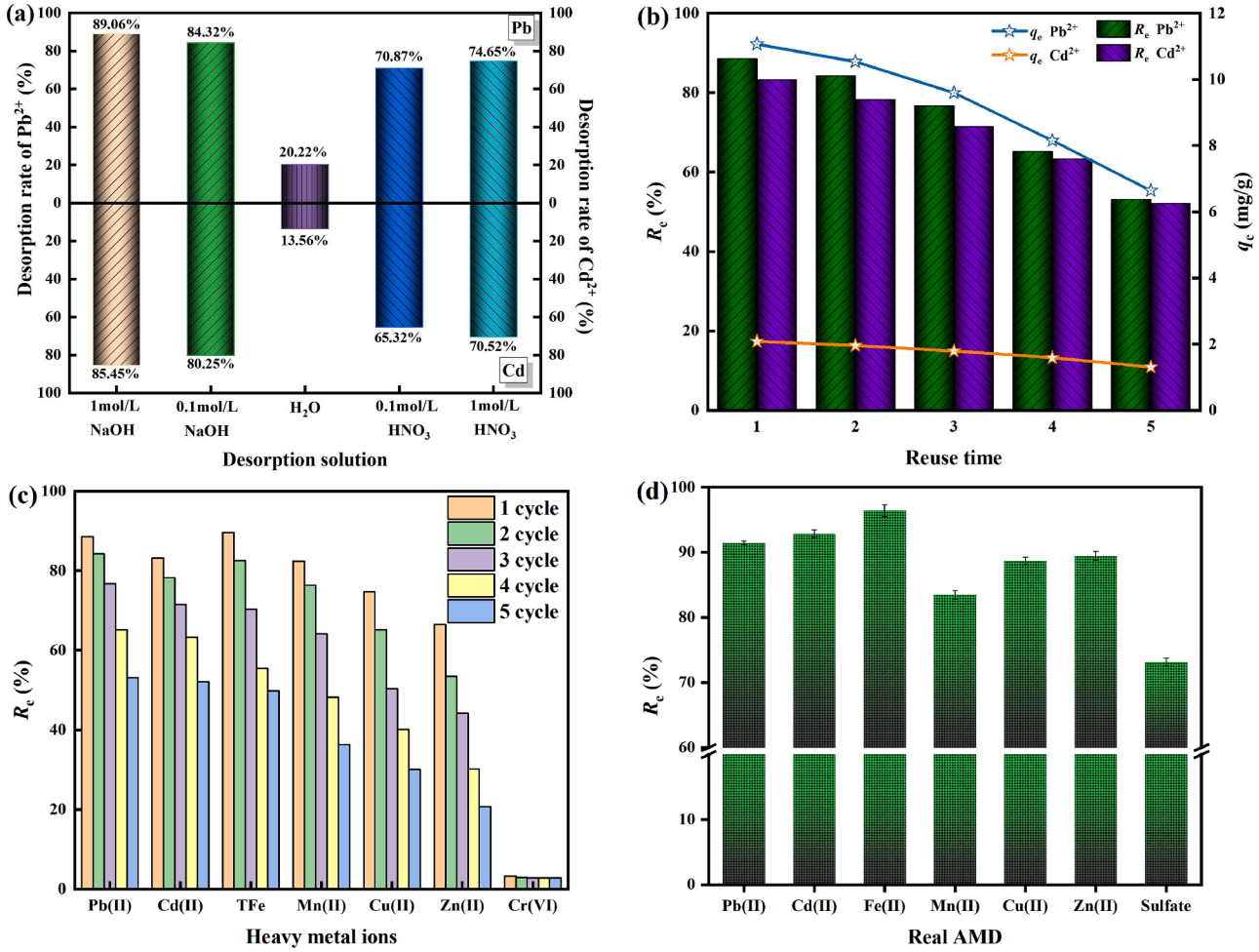

Fig. 8. The regeneration and utilization results of ROSL-G. (a) the desorption rate of Pb^{2+} and Cd^{2+}. (b) the regenerative capacity of ROSL-G. (c) the removal ability of heavy metal ions by ROSL-G. (d) the application potential of OSL-G in real AMD.

$(OH)_2$, $[Pb(OH)_4]^{2-}$, $[Pb_3(OH)_4]^{2+}$ and $Cd(OH)_2$ with Pb^{2+} and Cd^{2+}, which is conducive to the desorption of Pb^{2+} and Cd^{2+}.

The leachable heavy metal concentration of ROSL-G after 5 cycles can be used to indicate the potential toxicity of the sample. The leaching amounts of Pb^{2+} and Cd^{2+} in ROSL-G were 0.009 mg/L and 0.004 mg/L, respectively. On the one hand, heavy metals are fixed to the surface of the adsorbent in the form of oxides. On the other hand, the reaction of leached heavy metals with water is affected by the oxygen-containing functional groups on the surface of the adsorbent, forming surface complexes and being fixed (Pan et al., 2020). Therefore, ROSL-G after 5 cycles has lower toxic properties.

The adsorption–desorption experiment results of 1 mol/L NaOH solution for ROSL-G are shown in Fig. 8(b) to evaluate the reusability of OSL-G. It can be seen from Fig. 8(b), that after 5 times of adsorption–desorption, the removal rates of Pb^{2+} and Cd^{2+} in AMD by ROSL-G were still above 50 %, and the adsorption capacities were 6.6425 mg/g and 1.3033 mg/g, respectively. The adsorption capacity of ROSL-G to heavy metal ions after adsorption–desorption is shown in Fig. 8(c). It can be seen from Fig. 8(c), after 5 times of adsorption–desorption, the removal rates of Pb(II), Cd(II), TFe, Mn(II), Cu(II), Zn(II), and Cr(VI) by ROSL-G were 53.14 %, 52.13 %, 49.78 %, 36.25 %, 30.12 %, 20.71 %, and 2.82 %, respectively. After the reaction, there were red-brown, white, and blue precipitates in solutions. It shows that ROSL-G may depend on its alkalinity to change the heavy metal ions into hydroxide precipitation and remove. However, the effect of ROSL-G on the removal of Cr(VI) is small, indicating that ROSL-G does not have reducibility and can not be removed by turning Cr(VI) into Cr(III). Therefore, ROSL-G after adsorption–desorption is still valuable in the removal of other heavy metals, and it has a wide range of application values.

To explore the application potential of OSL-G, the adsorption experiment of OSL-G on real AMD was further carried out. It can be seen from Fig. 8(d), OSL-G has a good ability to treat heavy metal ions in real AMD, with removal rates ranging from 83 to 96 %. However, compared with simulated AMD, the removal rate was lower because of competitive adsorption between coexisting ions in real AMD. It was worth noting that the sulfate removal rate of OSL-G was lowest, because the removal of sulfate in AMD depended on not only adsorption, but also on the dissimilar reduction of sulfate reducing bacteria to convert it into metal sulfide.

4. Conclusions

In this paper, OSL-G was successfully prepared from lignite and oyster shells and used to remove Pb^{2+} and Cd^{2+} from simulated AMD. The addition of 4 g/L OSL-G can effectively treat AMD with pH 4 ~ 5 and initial Pb^{2+} and Cd^{2+} concentrations of 10 mg/L within 600 min. The OSL-G adsorption process conforms to the quasi-second-order kinetic model and the Freundlich model. The maximum adsorption capacity of Pb^{2+} and Cd^{2+} by OSL-G was 107.2821 mg/g and 8.3777 mg/g at 298.15 K, respectively. The adsorption process is a multistage-controlled spontaneous endothermic process. The mechanism of the adsorption of Pb^{2+} and Cd^{2+} by OSL-G is mainly the result of the synergistic effect of electrostatic adsorption, neutralization precipitation, ion exchange, and surface complexation. In addition, OSL-G is stable and has the potential

for reuse and good application. This study proposes a promising environmentally friendly adsorbent for AMD.

Funding

This work was supported by the Basic scientific research project of Liaoning Provincial Department of Education (JYTMS20230791), the National Natural Science Foundation of China (No. 41672247), Key Projects of Liaoning Provincial Department of Education (LJKZ0324), Project supported by discipline innovation team of Liaoning Technical University (No. LNTU20TD-21).

CRediT authorship contribution statement

Wenbo An: Conceptualization, Data curation, Formal analysis, Investigation, Methodology, Writing – original draft. **Yifan Liu:** Data curation, Methodology, Writing – original draft. **He Chen:** Data curation, Methodology, Writing – original draft. **Qiqi Wang:** Software, Methodology, Writing – original draft. **Xuechun Hu:** Software, Methodology, Writing – original draft. **Junzhen Di:** Conceptualization, Funding acquisition, Resources, Supervision, Validation, Methodology.

Declaration of competing interest

The authors declare that they have no known competing financial interests or personal relationships that could have appeared to influence the work reported in this paper.

Appendix A

The removal rate (R_e) and adsorption capacity (q_e) were calculated by Eqs. (A.1) and (A.2). Pseudo-first-order kinetics, pseudo-second-order kinetics, and intra-particle diffusion kinetics were used to fit the adsorption kinetic data of Pb^{2+} and Cd^{2+} by OSL-G. The fitting models are shown in Eqs. (A.3) ~ (A.5). Langmuir model and Freundlich model were used to fit the adsorption isotherm data of Pb^{2+} and Cd^{2+} by OSL-G. The fitting models are shown in Eqs. (A.6) and (A.7). Gibbs free energy ΔG, entropy change ΔH, and enthalpy change ΔS were used to describe the thermodynamic behavior of Pb^{2+} and Cd^{2+} by OSL-G. The thermodynamic parameters are shown in Eqs. (A.8)–(A.10). The desorption rate was calculated by Eq. (A.11).

$$R_e = \frac{C_0 - C_t}{C_0} \times 100\% \tag{A.1}$$

$$q_e = \frac{(C_0 - C_e) \times V}{M} \times 100\% \tag{A.2}$$

where R_e (%) is the removal rate, C_0 (mg/L) is the initial mass concentration, C_t (mg/L) is the mass concentration of the adsorbed substance in the solution at time t, q_e (mg/g) is the adsorption capacity at equilibrium, C_e (mg/L) is the mass concentration of the adsorbed substance in the solution at equilibrium, V (L) is the volume of the solution, and M (g) is the mass of OSL-G.

$$\ln(q_e - q_t) = \ln q_t - k_1 t \tag{A.3}$$

$$\frac{t}{q_t} = \frac{1}{k_2 q_e^2} + \frac{t}{q_e} \tag{A.4}$$

$$q_t = k_{idt} \cdot t^{0.5} + c \tag{A.5}$$

where q_e (mg/g) is the adsorption capacity at adsorption equilibrium, and q_t (mg/g) is the adsorption capacity at adsorption time t. k_1 (g/(mg·min)) is the reaction rate constant of the quasi-first-order kinetic model. k_2 (g/ (mg·min)) is the reaction rate constant of quasi-second-order kinetic model. k_{idt} (mg/ (g·$min^{0.5}$)) is the constant of the intra-particle diffusion model.

$$\frac{C_e}{q_e} = \frac{1}{q_m k_L} + \frac{C_e}{q_m} \tag{A.6}$$

$$\log q_e = \log k_F + \frac{1}{n} \log C_e \tag{A.7}$$

where C_e (mg/L) is the concentration of adsorbent in solution at equilibrium, q_e (mg/g) is the adsorption capacity at equilibrium, K_L (L/mg) and K_F (g/mg) are the coefficients of Langmuir model and Freundlich model, respectively. q_m (mg/g) is the maximum adsorption capacity, $1/n$ is the adsorption strength.

$$\Delta G = -RT\ln k \tag{A.8}$$

$$k = \frac{q_e}{C_e} \tag{A.9}$$

$$\ln k = \frac{-\Delta H}{RT} + \frac{\Delta S}{R} \tag{A.10}$$

where T (K) is the temperature of the adsorption system, R (8.314 J·mol^{-1}·K^{-1}) is the gas constant, k is the adsorption coefficient.

$$\eta = \frac{C \times V}{Q \times m} \tag{A.11}$$

where η (%) is the desorption rate, C (mg/L) is the ion concentration after desorption, V (L) is the volume of desorption solution, Q (mg/g) is the adsorption capacity of OSL-G on heavy metal ions, m (g) is the mass of OSL-G.

Appendix B

Table B1. BBD levels, test design and the responses.

Variation		Unit	Levels		
			Low (−1)	Central (0)	High (1)
A	Adhesive content	%	10	15	20
B	Roasting temperature	°C	500	600	700
C	Roasting time	h	1.5	2.0	2.5

Run	**Factors**			**Response values**				**Predicted values**			
	A	***B***	***C***	**$Pb^{2+}R_e$ (%)**	**$Cd^{2+}R_e$ (%)**	**Loss rate (%)**	**pH**	**$Pb^{2+}R_e$ (%)**	**$Cd^{2+}R_e$ (%)**	**Loss rate (%)**	**pH**
				Y_1	Y_2	Y_3	Y_4	Y_1	Y_2	Y_3	Y_4
1	10	500	2.0	99.84	96.07	100	7.23	99.83	96.06	100	7.23
2	30	500	2.0	99.78	87.16	67.09	6.52	99.78	87.05	66.42	6.64
3	10	700	2.0	99.95	99.84	53.68	9.99	99.95	99.95	54.35	9.87
4	30	700	2.0	99.76	93.23	21.63	8.42	99.77	93.24	21.27	8.42
5	10	600	1.5	99.91	97.01	46.92	7.66	99.92	96.74	48.6	7.72
6	30	600	1.5	99.76	91.03	2.87	6.67	99.76	90.86	5.59	6.6
7	10	600	2.5	99.9	97.93	29.58	7.08	99.9	98.1	26.87	7.15
8	30	600	2.5	99.84	87.99	4.52	6.29	99.83	88.26	2.84	6.23
9	20	500	1.5	99.75	94.96	92.91	6.98	99.75	95.24	90.87	6.93
10	20	700	1.5	99.78	99.69	56.1	9.36	99.78	99.86	53.75	9.43
11	20	500	2.5	99.75	94.38	84.74	6.81	99.76	94.21	87.09	6.75
12	20	700	2.5	99.82	99.94	31.01	8.62	99.82	99.66	33.05	8.67
13	20	600	2.0	99.85	96.56	4.28	6.82	99.87	96.71	5.74	6.76
14	20	600	2.0	99.88	95.92	3.44	6.69	99.87	96.71	5.74	6.76
15	20	600	2.0	99.9	96.78	8.13	6.71	99.87	96.71	5.74	6.76
16	20	600	2.0	99.88	97.38	7.81	6.85	99.87	96.71	5.74	6.76
17	20	600	2.0	99.86	96.91	5.03	6.74	99.87	96.71	5.74	6.76

Table B2. ANOVA results for adsorption of Pb^{2+} by OSL-G.

Source	*Sum of Squares*	*Degree of Freedom*	*Mean Square*	*F-value*	*P-value*	*significance*
Model	0.062	9	0.00693	26.29	0.0001	**
A	0.026	1	0.026	100.35	< 0.0001	**
B	0.00451	1	0.00451	17.12	0.0044	**
C	0.00151	1	0.00151	5.74	0.0478	*
AB	0.00423	1	0.00423	16.03	0.0052	**
AC	0.00203	1	0.00203	7.68	0.0276	*
BC	0.00040	1	0.00040	1.52	0.2578	
A^2	0.00136	1	0.00136	5.18	0.0571	
B^2	0.015	1	0.015	56.56	0.0001	**
C^2	0.00657	1	0.00657	24.92	0.0016	**
Residual	0.00185	7	0.000264			
Lack of Fit	0.000325	3	0.000108	0.29	0.8347	
Pure Error	0.00152	4	0.000380			
Cor Total	0.064	16				
R-Squared = 0.9713				*Pred R-Squared* = 0.8820		
		Adj R-Squared = 0 0.9343				
Adequate Precision = 15.962						
		C.V. % = 0.016				

Note: "" means significant ($P < 0.05$); "**" means extremely significant ($P < 0.01$).*

Table B3. ANOVA results for adsorption of Cd^{2+} by OSL-G.

Source	*Sum of Squares*	*Degree of Freedom*	*Mean Square*	*F-value*	*P-value*	*significance*
Model	224.09	9	24.9	109.88	< 0.0001	**
A	123.56	1	123.56	545.27	< 0.0001	**
B	50.65	1	50.65	223.53	< 0.0001	**
C	0.75	1	0.75	3.31	0.1116	
AB	1.32	1	1.32	5.84	0.0464	*

(*continued on next page*)

(*continued*)

Source	*Sum of Squares*	*Degree of Freedom*	*Mean Square*	*F-value*	*P-value*	*significance*
AC	3.92	1	3.92	17.3	0.0042	**
BC	0.17	1	0.17	0.76	0.4122	
A^2	42.95	1	42.95	189.53	< 0.0001	**
B^2	1.31	1	1.31	5.8	0.0469	*
C^2	0.00290	1	0.00290	0.013	0.9131	
Residual	1.59	7	0.23			
Lack of Fit	0.45	3	0.15	0.52	0.6903	
Pure Error	1.14	4	0.29			
Cor Total	225.68	16				
R-Squared = 0.9930				*Pred R-Squared* = 0.9605		
		Adj R-Squared = 0 0.9839				
Adequate Precision = 35.312						
		C.V. % = 0.50				

Note: "" means significant (P < 0.05); "**" means extremely significant (P < 0.01).*

Table B4. ANOVA results for loss rate of OSL-G.

Source	*Sum of Squares*	*Degree of Freedom*	*Mean Square*	*F-value*	*P-value*	*significance*
Model	18408.45	9	2045.38	243.27	< 0.0001	**
A	2246.85	1	2246.85	267.23	< 0.0001	**
B	4155.07	1	4155.07	494.18	< 0.0001	**
C	299.51	1	299.51	35.62	0.0006	**
AB	0.18	1	0.18	0.022	0.8863	
AC	90.16	1	90.16	10.72	0.0136	**
BC	71.57	1	71.57	8.51	0.0224	**
A^2	97.91	1	97.91	11.65	0.0112	**
B^2	10543.06	1	10543.06	1253.94	< 0.0001	**
C^2	456.48	1	456.48	54.29	0.0002	**
Residual	58.86	7	8.41			
Lack of Fit	40.93	3	13.64	3.05	0.1551	
Pure Error	17.92	4	4.48			
Cor Total	18467.31	16				
R-Squared = 0.9968				*Pred R-Squared* = 0.9630		
		Adj R-Squared = 0.9927				
Adequate Precision = 43.851						
		C.V. % = 7.95				

Note: "" means significant (P < 0.05); "**" means extremely significant (P < 0.01).*

Table B5. ANOVA results for pH of the solution.

Source	*Sum of Squares*	*Degree of Freedom*	*Mean Square*	*F-value*	*P-value*	*significance*
Model	18.31	9	2.03	181.06	< 0.0001	**
A	2.06	1	2.06	183.37	< 0.0001	**
B	9.79	1	9.79	871.3	< 0.0001	**
C	0.44	1	0.44	38.9	0.0004	**
AB	0.18	1	0.18	16.46	0.0048	**
AC	0.01	1	0.01	0.89	0.3769	
BC	0.081	1	0.081	7.23	0.0311	*
A^2	0.071	1	0.071	6.36	0.0397	*
B^2	5.55	1	5.55	493.63	< 0.0001	**
C^2	0.00452	1	0.00452	0.4	0.5463	
Residual	0.079	7	0.011			
Lack of Fit	0.059	3	0.02	4.05	0.1050	
Pure Error	0.019	4	0.004875			
Cor Total	18.39	16				
R-Squared = 0.9957			*Adj R-Squared* = 0.9902	*Pred R-Squared* = 0.9469		
Adequate Precision = 44.711			*C.V. %* = 1.44			

References

Abdelsayed, V., Shekhawat, D., Smith, M.W., Link, D., Stiegman, A.E., 2018. Microwaveassisted pyrolysis of Mississippi coal: a comparative study with conventional pyrolysis. Fuel 217, 656–667. https://doi.org/10.1016/j.fuel.2017.12.099.

Akinwekomi, V., Maree, J.P., Masindi, V., Zvinowanda, C., Osman, M.S., Foteinis, S., Mpenyana-Monyatsi, L., Chatzisymeon, E., 2020. Beneficiation of acid mine drainage (AMD): A viable option for the synthesis of goethite, hematite, magnetite, and gypsum-Gearing towards a circular economy concept. Miner. Eng. 148, 106204 https://doi.org/10.1016/j.mineng.2020.106204.

Alakangas, L., Andersson, E., Mueller, S., 2013. Neutralization/prevention of acid rock drainage using mixtures of alkaline by-products and sulfidic mine wastes. Environ. Sci. Pollut. Res. 20 (11), 7907–7916. https://doi.org/10.1007/s11356-013-1838-z.

Alastair, M., Andrew, H., Pascaline, P., Mark, E., Pete, W., 2018. Alkali activation behaviour of un-calcined montmorillonite and illite clay minerals. Appl. Clay Sci. 166, 250–261. https://doi.org/10.1016/j.clay.2018.09.011.

Alidoust, D., Kawahigashi, M., Yoshizawa, S., Sumida, H., Watanabe, M., 2015. Mechanism of cadmium biosorption from aqueous solutions using calcined oyster

shells. J. Environ. Manage. 150, 103–110. https://doi.org/10.1016/j.jenvman.2014.10.032.
Arslanoglu, H., Kaya, S., Tümen, F., 2019. Cr(VI) adsorption on low-cost activated carbon developed from grape marc-vinasse mixture. Part. Sci. Technol. 38 (6), 768–781. https://doi.org/10.1080/02726351.2019.1632399.
Awang, N.A., Salleh, W.N.W., Ismail, A.F., Yusof, N., Aziz, F., Jaafar, J., 2019. Adsorption behavior of chromium(VI) onto regenerated cellulose membrane. Ind. Eng. Chem. Res. 58 (2), 720–728. https://doi.org/10.1021/acs.iecr.8b02366.
Bai, B., Bai, F., Sun, C.M., Nie, Q.K., Sun, S., 2023. Adsorption mechanism of shell powders on heavy metal ions Pb2+/Cd2+ and the purification efficiency for contaminated soils. Front. Earth Sci. 10, 1071228. https://doi.org/10.3389/feart.2022.1071228.
Bai, J.C., Zhang, H.Q., Xiao, L.P., 2021. Formation mechanism of carbide slag composite sustained-alkalinity-release particles for the source control of acid mine drainage. Sci. Rep. 11 (01), 23793. https://doi.org/10.1038/s41598-021-03277-w.
Bao, S.H., Di, J.Z., Yang, J.G., Wang, D.L., Sun, J., Dong, Y.R., 2021. Experimental study on adsorption characteristics of Cu2+ and Zn2+ by datong lignite. Environ. Eng. Res. 27 (3), 210037 https://doi.org/10.4491/eer.2021.037.
Bartczak, P., Norman, M., Klapiszewski, L., Karwanska, N., Kawalec, M., Baczynska, M., Wysokowski, M., Zdarta, J., Ciesielczyk, F., Jesionowski, T., 2018. Removal of nickel (II) and lead(II) ions from aqueous solution using peat as a low-cost adsorbent: A kinetic and equilibrium study. Arab. J. Chem. 11 (8), 1209–1222. https://doi.org/10.1016/j.arabjc.2015.07.018.
Bohli, T., Ouederni, A., Fiol, N., Villaescusa, I., 2015. Single and binary adsorption of some heavy metal ions from aqueous solutions by activated carbon derived from olive stones. Desalin. Water Treat. 53 (4), 1082–1088. https://doi.org/10.1080/19443994.2013.859099.
Cao, B., Qu, J.H., Yuan, Y.H., Zhang, W.H., Miao, X.M., Zhang, X.R., Xu, Y., Han, T.Y., Song, H.J., Ma, S.Y., Tian, X., Zhang, Y., 2022. Efficient scavenging of aqueous Pb (II)/Cd(II) by sulfide-iron decorated biochar: performance, mechanisms and reusability exploration. J. Environ. Chem. Eng. 10 (3), 107531 https://doi.org/10.1016/j.jece.2022.107531.
Cheng, S., Meng, W.B., Xing, B.L., Shi, C.L., Wang, Q., Xia, D.P., Nie, Y.H., Yi, G.Y., Zhang, C.X., Xia, H.Y., 2023b. Efficient removal of heavy metals from aqueous solutions by Mg/Fe bimetallic oxide-modified biochar: experiments and DFT investigations. J. Clean. Prod. 403, 136821 https://doi.org/10.1016/j.jclepro.2023.136821.
Cheng, J.G., Zhang, S.F., Fang, C., Ma, L.T., Duan, J.G., Fang, X., Li, R.H., 2023a. Removal of heavy metal ions from aqueous solution using biotransformed lignite. Molecules 28 (13), 5031. https://doi.org/10.3390/molecules28135031.
Cherdchoo, W., Nithettham, S., Charoenpanich, J., 2019. Removal of Cr(VI) from synthetic wastewater by adsorption onto coffee ground and mixed waste tea. Chemosphere 221, 758–767. https://doi.org/10.1016/j.chemosphere.2019.01.100.
Du, T.H., Bogush, A., Edwards, P., Stanley, P., Lombardi, A.T., Campos, L.C., 2022. Bioaccumulation of metals by algae from acid mine drainage: a case study of Frongoch Mine (UK). Environ. Sci. Pollut. Res. 29 (21), 32261–32270. https://doi.org/10.1007/s11356-022-19604-1.
Du, Y., Lian, F., Zhu, L.Y., 2011. Biosorption of divalent Pb, Cd and Zn on aragonite and calcite mollusk shells. Environ. Pollut. 159 (7), 1763–1768. https://doi.org/10.1016/j.envpol.2011.04.017.
El Atouani, S., Belattmania, Z., Reani, A., Tahiri, S., Aarfane, A., Bentiss, F., Jama, C., Zrid, R., Sabour, B., 2019. Brown seaweed sargassum muticum as low-cost biosorbent of methylene blue. Int. J. Environ. Res. 13 (1), 131–142. https://doi.org/10.1007/s41742-018-0161-4.
Feng, M.H., Li, M.M., Zhang, L.S., Luo, Y., Zhao, D., Yuan, M.Y., Zhang, K.Q., Wang, F., 2022. Oyster shell modified tobacco straw biochar: efficient phosphate adsorption at wide range of pH values. Int. J. Environ. Res. Public Health 19 (12), 7227. https://doi.org/10.3390/ijerph19127227.
Frišták, V., Pipíška, M., Lesný, J., Soja, G., Wolfgang Friesl-Hanl, W., Packová, A., 2015. Utilization of biochar sorbents for Cd2+, Zn2+, and Cu2+ ions separation from aqueous solutions: comparative study. Environ. Monit. Assess. 187 (1), 4093. https://doi.org/10.1007/s10661-014-4093-y.
Gameli, R.B.H., Alhassan, E.H., Duwiejuah, A.B., Abarike, E.D., Bawa, A.A., 2023. Binary and ternary metals adsorption from greywater using spent green tea as a novel adsorbent. Afr. J. Sci. 119 (7–8), 13352. https://doi.org/10.17159/sajs.2023/13352.
Ha, S., Lee, J.W., Choi, S.H., Kim, S.H., Kim, K., Kim, Y., 2019. Calcination characteristics of oyster shells and their comparison with limestone from the perspective of waste recycling. J. Mater. Cycles Waste Manage. 21 (05), 1075–1084. https://doi.org/10.1007/s10163-019-00860-2.
Hao, L.P., Gao, W.Y., Yan, S., Niu, M.H., Liu, G.S., Hao, H.S., 2019. Preparation and characterization of porous ceramics with low-grade diatomite and oyster shell. Mater. Chem. Phys. 235, 121741 https://doi.org/10.1016/j.matchemphys.2019.121741.
He, X., Zeng, K., Xie, Y.P., Flamant, G., Yang, H.P., Yang, X.Y., Nzihou, A., Zheng, A.Q., Ding, Z., Chen, H.P., 2019. The effects of temperature and molten salt on solar pyrolysis of lignite. Energy 181, 407–416. https://doi.org/10.1016/j.energy.2019.05.181.
Homagai, P.L., Poudel, R., Poudel, S., Bhattarai, A., 2022. Adsorption and removal of crystal violet dye from aqueous solution by modified rice husk. Heliyon 8 (4), e09261.
Hsu, T.C., 2009. Experimental assessment of adsorption of Cu2+ and Ni2+ from aqueous solution by oyster shell powder. J. Hazard. Mater. 171 (1–3), 995–1000. https://doi.org/10.1016/j.jhazmat.2009.06.105.
Huang, R.L., Lin, Q.T., Zhong, Q.F., Zhang, X.F., Wen, X.Q., Luo, H.Y., 2020. Removal of Cd(II) and Pb(II) from aqueous solution by modified attapulgite clay. Arab. J. Chem. 13 (4), 4994–5008. https://doi.org/10.1016/j.arabjc.2020.01.022.
Huang, B., Liu, G.W., Wang, P.H., Zhao, X., Xu, H.X., 2019. Effect of nitric acid modification on characteristics and adsorption properties of lignite. Processes 7 (3), 167. https://doi.org/10.3390/pr7030167.
Iakovleva, E., Mäkilä, E., Salonen, J., Sitarz, M., Wang, S.B., Sillanpää, M., 2015. Acid mine drainage (AMD) treatment: neutralization and toxic elements removal with unmodified and modified limestone. Ecol. Eng. 81, 30–40. https://doi.org/10.1016/j.ecoleng.2015.04.046.
Jamshidifard, S., Koushkbaghi, S., Hosseini, S., Rezaei, S., Karamipour, A., Rad, A.J., Irani, M., 2019. Incorporation of UiO-66-NH2 MOF into the PAN/chitosan nanofibers for adsorption and membrane filtration of Pb(II), Cd(II) and Cr(VI) ions from aqueous solutions. J. Hazard. Mater. 368, 10–20. https://doi.org/10.1016/j.jhazmat.2019.01.024.
Jellali, S., Azzaz, A.A., Jeguirim, M., Hamdi, H., Mlayah, A., 2021. Use of lignite as a low-cost material for cadmium and copper removal from aqueous solutions: assessment of adsorption characteristics and exploration of involved mechanisms. Water. 13 (2), 164. https://doi.org/10.3390/w13020164.
Jiang, J., Long, Y.C., Hu, X.J., Hu, J., Zhu, M.S., Zhou, S.Q., 2020. A facile microwave-assisted synthesis of mesoporous hydroxyapatite as an efficient adsorbent for Pb2+ adsorption. J. Solid State Chem. 289, 121491 https://doi.org/10.1016/j.jssc.2020.121491.
Kacakgil, E.C., Cetintas, S., 2021. Preparation and characterization of a novel functionalized agricultural waste-based adsorbent for Cu2+ removal: evaluation of adsorption performance using response surface methodology. Sustain. Chem. Pharm. 22, 100468 https://doi.org/10.1016/j.scp.2021.100468.
Khan, M.D., Ahn, J.W., Nam, G., 2018. Environmental benign synthesis, characterization and mechanism studies of green calcium hydroxide nano-plates derived from waste oyster shells. J. Environ. Manage. 223, 947–951. https://doi.org/10.1016/j.jenvman.2018.07.011.
Kim, W., Singh, R., 2022. Modified oyster waste shells as a value-added sorbent for lead removal from water. Bull. Environ. Contam. Toxicol. 108 (3), 518–525. https://doi.org/10.1007/s00128-021-03133-7.
Kolodynska, D., Wnetrzak, R., Leahy, J.J., Hayes, M.H.B., Kwapinski, W., Hubicki, Z., 2012. Kinetic and adsorptive characterization of biochar in metal ions removal. Chem. Eng. J. 197, 295–305. https://doi.org/10.1016/j.cej.2012.05.025.
Lee, Y., Ren, Y., Cui, M., Zhou, Y., Kwon, O., Ko, J., Khim, J., 2022. Arsenic adsorption study in acid mine drainage using fixed bed column by novel beaded adsorbent. Chemosphere 291 (3), 132894. https://doi.org/10.1016/j.chemosphere.2021.132894.
Li, P.G., Fu, T., Gao, X.Y., Zhu, W.J., Han, C.Y., Liu, N.S., He, S.F., Luo, Y.M., Ma, W.H., 2019. Adsorption and reduction transformation behaviors of Cr(VI) on mesoporous polydopamine/titanium dioxide composite nanospheres. J. Chem. Eng. Data 64 (6), 2686–2696. https://doi.org/10.1021/acs.jced.9b00111.
Li, A.Y., Ge, W.Z., Liu, L.H., Zhang, Y.T., Qiu, G.H., 2022. Synthesis and application of amine-functionalized MgFe2O4-biochar for the adsorption and immobilization of Cd (II) and Pb(II). Chem. Eng. J. 439, 135785 https://doi.org/10.1016/j.cej.2022.135785.
Li, G.Y., Xu, X.Y., Chen, E., Fan, J., Xiong, G.J., 2015. Properties of cement-based bricks with oyster-shells ash. J. Clean. Prod. 91, 279–287. https://doi.org/10.1016/j.jclepro.2014.12.023.
Li, B., Yang, L., Wang, C.Q., Zhang, Q.P., Liu, Q.C., Li, Y.D., Xiao, R., 2017. Adsorption of Cd(II) from aqueous solutions by rape straw biochar derived from different modification processes. Chemosphere 175, 332–340. https://doi.org/10.1016/j.chemosphere.2017.02.061.
Li, Z.B., Zhao, S.Y., Zhao, X.G., He, T.S., 2012. Leaching characteristics of steel slag components and their application in cementitious property prediction. J. Hazard. Mater. 199, 448–452. https://doi.org/10.1016/j.jhazmat.2011.07.069.
Liang, Q.W., Luo, H.J., Geng, J.J., Chen, J.D., 2018. Facile one-pot preparation of nitrogen-doped ultra-light graphene oxide aerogel and its prominent adsorption performance of Cr(VI). Chem. Eng. J. 338, 62–71. https://doi.org/10.1016/j.cej.2017.12.145.
Lin, C., Luo, W.J., Luo, T.T., Zhou, Q., Li, H.F., Jing, L.R., 2018. A study on adsorption of Cr (VI) by modified rice straw: characteristics, performances and mechanism. J. Clean. Prod. 196, 626–634. https://doi.org/10.1016/j.jclepro.2018.05.279.
Liphadzi, S.M., Vermaak, A.P., 2017. Assessment of employees' perceptions of approaches to sustainable water management by coal and iron ore mining companies. J. Clean. Prod. 153 (1), 608–625. https://doi.org/10.1016/j.jclepro.2015.01.037.
Liu, X.F., Dong, X.Q., Chang, S.Q., Xu, X., Li, J.S., Pu, H.F., 2023. Remediation of lead-contaminated groundwater by oyster shell powder-peanut shell biochar mixture. Environ. Geochem. Health. https://doi.org/10.1007/s10653-023-01756-9.
Liu, L.H., Liu, X., Wang, D.Q., Lin, H., Huang, L., 2020. Removal and reduction of Cr(VI) in simulated wastewater using magnetic biochar prepared by co-pyrolysis of nano-zero-valent iron and sewage sludge. J. Clean. Prod. 257, 120562 https://doi.org/10.1016/j.jclepro.2020.120562.
Liu, Y., Sun, C.B., Xu, J., Li, Y.Z., 2009. The use of raw and acid-pretreated bivalve mollusk shells to remove metals from aqueous solutions. J. Hazard. Mater. 168 (1), 156–162. https://doi.org/10.1016/j.jhazmat.2009.02.009.
Lu, J.S., Cong, X.Q., Li, Y.D., Hao, Y., Wang, C.L., 2018. Scalable recycling of oyster shells into high purity calcite powders by the mechanochemical and hydrothermal treatments. J. Clean. Prod. 172, 1978–1985. https://doi.org/10.1016/j.jclepro.2017.11.228.
Luo, L., Wang, G.L., Wang, Z.M., Ma, J.H., He, Y., He, J.S., Wang, L.L., Liu, Y., Xiao, H., Xiao, Y.L., Lan, T., Yang, H., Deng, O.P., 2021. Optimization of Fenton process on

removing antibiotic resistance genes from excess sludge by single-factor experiment and response surface methodology. Sci. Total Environ. 788, 147889 https://doi.org/10.1016/j.scitotenv.2021.147889.
Madrid, J.A., Lanzon, M., 2017. Synthesis and morphological examination of high-purity Ca(OH)(2) nanoparticles suitable to consolidate porous surfaces. Appl. Surf. Sci. 424 (SI), 2–8. https://doi.org/10.1016/j.apsusc.2017.03.210.
Maree, J.P., Mujuru, M., Bologo, V., Daniels, N., Mpholoane, D., 2013. Neutralisation treatment of AMD at affordable cost. Water SA 39 (2), 245–250. https://doi.org/10.4314/wsa.v39i2.7.
Melo, C.R., Riella, H.G., Kuhnen, N.C., Melo, A.R., Rocha, M.R., Mendes, E., Antunes, L., Angioletto, E., 2015. Adsorption of iron and manganese from acid mine drainage using 4A-zeolite synthesised from waste with high kaolin concentrations. Int. J. Environ. Pollut. 56 (1–4), 79–93. https://doi.org/10.1504/IJEP.2014.067682.
Mlayah, A., Jellali, S., Azzaz, A.A., Jeguirim, M., Sellalmi, H., Hamdi, N., 2021. Investigations on lignite use for lead removal from aqueous solutions under static and dynamic conditions: adsorption properties and mechanism exploration. C. R. Chim. 24, 7–22. https://doi.org/10.5802/crchim.71.
Mo, W., He, Q.Z., Su, X.J., Ma, S.J., Feng, J.P., He, Z.L., 2018. Preparation and characterization of a granular bentonite composite adsorbent and its application for Pb2+ adsorption. Appl. Clay Sci. 159 (SI), 68–73. https://doi.org/10.1016/j.clay.2017.12.001.
Moon, D.H., Cheong, K.H., Khim, J., Wazne, M., Hyun, S., Park, J.H., Chang, Y.Y., Ok, Y. S., 2013. Stabilization of Pb2+ and Cu2+ contaminated firing range soil using calcined oyster shells and waste cow bones. Chemosphere 91 (9), 1349–1354. https://doi.org/10.1016/j.chemosphere.2013.02.007.
Mousavi, S.J., Parvini, M., Ghorbani, M., 2018. Adsorption of heavy metals (Cu2+ and Zn2+) on novel bifunctional ordered mesoporous silica: optimization by response surface methodology. J. Taiwan Inst. Chem. Eng. 84, 123–141. https://doi.org/10.1016/j.jtice.2018.01.010.
Nazari, S., Rahimi, G., Nezhad, A.K.J., 2019. Effectiveness of native and citric acid-enriched biochar of Chickpea straw in Cd and Pb sorption in an acidic soil. J. Environ. Chem. Eng. 7 (2), 103064 https://doi.org/10.1016/j.jece.2019.103064.
Nkuna, C.N., Sadiku, E.R., Perry, G., Oboirien, B., Dludlu, M.K., Thompson, C., 2023. Treatment of acid mine drainage and chromium (VI) removal using synthesised chitosan composites blended with kenaf fibre and γ-Fe2O3 nanoparticles. Int. J. Environ. Sci. Technol. 20 (4), 3599–3612. https://doi.org/10.1007/s13762-022-04243-3.
Ogata, F., Ueta, E.i., Kawasaki, N., 2018. Characteristics of a novel adsorbent Fe-Mgtype hydrotalcite and its adsorption capability of As(III) and Cr(VI) from aqueous solution. J. Ind. Eng. Chem. 59, 56–63. https://doi.org/10.1016/j.jiec.2017.10.005.
Okano, K., Uemoto, M., Kagami, J., Miura, K., Miura, K., Toda, M., Honda, K., Ohtake, H., 2013. Novel technique for phosphorus recovery from aqueous solutions using amorphous calcium silicate hydrates (A-CSHs). Water Res. 47 (7), 2251–2259. https://doi.org/10.1016/j.watres.2013.01.052.
Pan, J.W., Gao, B.Y., Wang, S.Y., Guo, K.Y., Xu, X., Yue, Q.Y., 2020. Waste-to-resources: green preparation of magnetic biogas residues-based biochar for effective heavy metal removals. Sci. Total Environ. 737, 140283 https://doi.org/10.1016/j.scitotenv.2020.140283.
Pehlivan, E., Yanık, B.H., Ahmetli, G., Pehlivan, M., 2008. Equilibrium isotherm studies for the uptake of cadmium and lead ions onto sugar beet pulp. Bioresour. Technol. 99 (9), 3520–3527. https://doi.org/10.1016/j.biortech.2007.07.052.
Pérez, B.F., Espina, J.A., González, M.D.F., 2022. Adsorption of heavy metals ions from mining metallurgical tailings leachate using a shell-based adsorbent: characterization, kinetics and isotherm studies. Materials 15 (15), 5315. https://doi.org/10.3390/ma15155315.
Ren, J.J., Zheng, L.C., Su, Y.M., Meng, P.P., Zhou, Q.Y., Zeng, H., Zhang, T., Yu, H.J., 2022. Competitive adsorption of Cd(II), Pb(II) and Cu(II) ions from acid mine drainage with zero-valent iron/phosphoric titanium dioxide: XPS qualitative analyses and DFT quantitative calculations. Chem. Eng. J. 445, 136778 https://doi.org/10.1016/j.cej.2022.136778.
Rodríguez-Galán, M., Baena-Moreno, F.M., Vázquez, S., Arroyo-Torralvo, F., Vilches, L. F., Zhang, Z.E., 2019. Remediation of acid mine drainage. Environ. Chem. Lett. 17 (4), 1529–1538. https://doi.org/10.1007/s10311-019-00894-w.
Saeed, A.A.H., Harun, N.Y., Sufian, S., Bilad, M.R., Nufida, B.A., Ismail, N.M., Zakaria, Z. Y., Jagaba, A.H., Ghaleb, A.A.S., Al-Dhawi, B.N.S., 2021. Modeling and optimization of biochar based adsorbent derived from kenaf using response surface methodology on adsorption of Cd^2+. Water 13 (7), 999. https://doi.org/10.3390/w13070999.
Samanta, A., Chanda, D.K., Das, P.S., Ghosh, J., Dey, A., Das, S., Mukhopadhyay, A.K., 2016a. Synthesis of mixed calcite-calcium oxide nanojasmine flowers. Ceram. Int. 42, 2339–2348. https://doi.org/10.1016/j.ceramint.2015.10.030.
Samanta, A., Chanda, D.K., Das, P.S., Ghosh, J., Mukhopadhyay, A.K., Dey, A., 2016b. Synthesis of nano calcium hydroxide in aqueous medium. J. Am. Ceram. Soc. 99, 787–795. https://doi.org/10.1111/jace.14023.
Samanta, A., Podder, S., Ghosh, C.K., Bhattacharya, M., Ghosh, J., Mallik, A.K., Dey, A., Mukhopadhyay, A.K., 2017. ROS mediated high antibacterial efficacy of strain tolerant layered phase pure nano-calcium hydroxide. J. Mech. Behav. Biomed. Mater. 72, 110–128. https://doi.org/10.1016/j.jmbbm.2017.04.004.
Shi, Y., Xing, Y.F., Song, Z.L., Dang, X.M., Zhao, H.M., 2022. Adsorption performance and its mechanism of aqueous As(III) on polyporous calcined oyster shell-supported Fe-Mn binary oxide. Water Environ. Res 94 (4), e10714.
Sun, C., Chen, T., Huang, Q.X., Wang, J., Lu, S.Y., Yan, J.H., 2019. Enhanced adsorption for Pb(II) and Cd(II) of magnetic rice husk biochar by KMnO4 modification. Environ. Sci. Pollut. Res. 26 (9), 8902–8913. https://doi.org/10.1007/s11356-019-04321-z.
Sun, Y.J., Ma, J., Chen, Y.G., Tan, B.H., Cheng, W.J., 2020. Mechanical behavior of copper-contaminated soil solidifed/stabilized with carbide slag and metakaolin. Environ. Earth Sci. 79 (18), 423. https://doi.org/10.1007/s12665-020-09172-3.
Sun, L., Yuan, Z.G., Gong, W.B., Zhang, L.D., Xu, Z.L., Su, G.B., Han, D.G., 2015. The mechanism study of trace Cr(VI) removal from water using Fe0 nanorods modified with chitosan in porous anodic alumina. Appl. Surf. Sci. 328, 606–613. https://doi.org/10.1016/j.apsusc.2014.12.094.
Suwannasingha, N., Kantavong, A., Tunkijjanukij, S., Aenglong, C., Liu, H.B., Klaypradit, W., 2022. Effect of calcination temperature on structure and characteristics of calcium oxide powder derived from marine shell waste. J. Saudi Chem. Soc. 26 (02), 101441 https://doi.org/10.1016/j.jscs.2022.1014411319-6103.
Tamjidi, S., Ameri, A., 2020. A review of the application of sea material shells as low cost and effective bio-adsorbent for removal of heavy metals from wastewater. Environ. Sci. Pollut. Res. 27 (25), 31105–31119. https://doi.org/10.1007/s11356-020-09655-7.
Tho, P.T., Van, H.T., Nguyen, L.H., Hoang, T.K., Tran, T.N.H., Nguyen, T.T., Nguyen, T.B. H., Nguyen, V.Q., Sy, H.L., Thai, V.N., Tran, Q.B., Sadeghzadeh, S.M., Asadpour, R., Thang, P.Q., 2021. Enhanced simultaneous adsorption of As(iii), Cd(ii), Pb(ii) and Cr (vi) ions from aqueous solution using cassava root husk-derived biochar loaded with ZnO nanoparticles. RSC Adv. 11 (31), 18881–18897. https://doi.org/10.1039/d1ra01599k.
Tudor, H.E.A., Gryte, C.C., Harris, C.C., 2006. Seashells: detoxifying agents for metal-contaminated waters. Water Air Soil Pollut. 173 (1–4), 209–242. https://doi.org/10.1007/s11270-005-9060-3.
Upadhyay, U., Sreedhar, I., Singh, S.A., Patel, C.M., Anitha, K.L., 2021. Recent advances in heavy metal removal by chitosan based adsorbents. Carbohydr. Polym. 251, 117000 https://doi.org/10.1016/j.carbpol.2020.117000.
Wan, S.L., Ma, Z.Z., Xue, Y., Ma, M.H., Xu, S.Y., Qian, L.P., Zhang, Q.R., 2014. Sorption of lead (II), cadmium (II) and copper (II) ions from aqueous solution using tea waste. Ind. Eng. Chem. Res. 53 (9), 3629–3635. https://doi.org/10.1021/ie402510s.
Wang, P., Huang, Z.B., Fu, Z.Y., Zhao, P., Feng, Z.S., Wang, Y., Li, F.Z., 2022. Adsorption mechanism of Cd(II) by calcium-modified lignite-derived humin in aqueous solutions. Int. J. Coal Sci. Technol. 9 (1), 37. https://doi.org/10.1007/s40789-022-00492-2.
Wang, F.D., Li, J., Su, Y., Li, Q., Gao, B.Y., Yue, Q.Y., Zhou, W.Z., 2019. Adsorption and recycling of Cd(II) from wastewater using straw cellulose hydrogel beads. J. Ind. Eng. Chem. 80, 361–369. https://doi.org/10.1016/j.jiec.2019.08.015.
Wang, Q.A., Yan, P.Y., Feng, J.W., 2011. A discussion on improving hydration activity of steel slag by altering its mineral compositions. J. Hazard. Mater. 186 (2–3), 1070–1075. https://doi.org/10.1016/j.jhazmat.2010.11.109.
Xia, C.H., Zhang, X.Y., Xia, L.H., 2021. Heavy metal ion adsorption by permeable oyster shell bricks. Constr. Build. Mater. 275, 122128 https://doi.org/10.1016/j.conbuildmat.2020.122128.
Xu, X., Liu, X.F., Oh, M., Park, J., 2019. Oyster shell as a low-cost adsorbent for removing heavy metal ions from wastewater. Pol. J. Environ. Stud. 28 (4), 2949–2959. https://doi.org/10.15244/pjoes/92941.
Xu, Z.Y., Valeo, C., Chu, A.G., Zhao, Y., 2021. The efficacy of whole oyster shells for removing copper, zinc, chromium, and cadmium heavy metal ions from stormwater. Sustainability 13 (08), 4184. https://doi.org/10.3390/su13084184.
Yen, H.Y., Li, J.Y., 2015. Process optimization for Ni(II) removal from wastewater by calcined oyster shell powders using Taguchi method. J. Environ. Manage. 161, 344–349. https://doi.org/10.1016/j.jenvman.2015.07.024.
Zaman, H.G., Baloo, L., Kutty, S.R., Altaf, M., 2023. Post synthetic modification of NH2-(Zr-MOF) via rapid microwave-promoted synthesis for effective adsorption of Pb(II) and Cd(II). Arab. J. Chem. 16 (1), 104122 https://doi.org/10.1016/j.arabjc.2022.104122.
Zendelska, A., Golomeova, M., Golomeov, B., Krstev, B., 2018. Removal of lead ions from acid aqueous solutions and acid mine drainage using zeolite bearing tuff. Arch. Environ. Protect. 44 (1), 87–96. https://doi.org/10.24425/118185.
Zhan, X.H., Xiao, L.P., Liang, B., 2020. Experimental study on the optimum preparation of bentonite-steel slag composite particles. Sustainability 12 (01), 18. https://doi.org/10.3390/su12010018.
Zhang, B., Chen, Y.L., 2020. Particle size effect on pore structure characteristics of lignite determined via low-temperature nitrogen adsorption. J. Nat. Gas Sci. Eng. 84, 103633 https://doi.org/10.1016/j.jngse.2020.103633.
Zhang, K., Li, Y., Wang, Z.H., Li, Q., Whiddon, R., He, Y., Cen, K.F., 2016. Pyrolysis behavior of a typical Chinese sub-bituminous Zhundong coal from moderate to high temperatures. Fuel 185, 701–708. https://doi.org/10.1016/j.fuel.2016.08.038.
Zhang, Y., Li, M., Li, J.C., Yang, Y.Y., Liu, X., 2019. Surface modified leaves with high efficiency for the removal of aqueous Cr (VI). Appl. Surf. Sci. 484, 189–196. https://doi.org/10.1016/j.apsusc.2019.04.088.
Zhang, W., Liu, X.M., Zhang, Z.Q., Li, Y.T., Gu, J.R., 2022. Synergic effects of circulating fluidized bed fly ash-red mud-blast furnace slag in green cementitious materials: hydration products and environmental performance. J. Build. Eng. 58, 105007 https://doi.org/10.1016/j.jobe.2022.105007.
Zhang, C.H., Luo, B., Xu, Z.M., Sun, Y.J., Feng, L., 2023a. Research on the capacity of underground reservoirs in coal mines to protect the groundwater resources: a case of Zhangshuanglou coal mine in Xuzhou, China. Water 15 (8), 1468. https://doi.org/10.3390/w15081468.
Zhang, T.T., Wang, W., Zhao, Y.L., Bai, H.Y., Wen, T., Kang, S.C., Song, G.S., Song, S.X., Komarneni, S., 2021. Removal of heavy metals and dyes by clay-based adsorbents: from natural clays to 1D and 2D nano-composites. Chem. Eng. J. 420 (2), 127574 https://doi.org/10.1016/j.cej.2020.127574.
Zhang, W., You, Q.Z., Shu, J.K., Wang, A.H., Lin, H., Yan, X.C., 2023b. Optimization of preparation conditions of modified oyster shell Powder/Ce-N-TiO2 by response surface methodology (RSM). J. Environ. Prot. 14 (01), 16–31. https://doi.org/10.4236/jep.2023.141002.

Zhong, G.S., Liu, Y.S., Tang, Y.Y., 2021. Oyster shell powder for Pb(II) immobilization in both aquatic and sediment environments. Environ. Geochem. Health 43, 1891–1902. https://doi.org/10.1007/s10653-020-00768-z.

Zhou, Z.F., Wang, Y.N., Sun, S., Wang, Y.C., Xu, L., 2022. Preparation of PVA/waste oyster shell powder composite as an efficient adsorbent of heavy metals from wastewater. Heliyon 8 (12), e11938.

Znad, H., Awual, M.R., Martini, S., 2022. The utilization of algae and seaweed biomass for bioremediation of heavy metal-contaminated wastewater. Molecules 27 (4), 1275. https://doi.org/10.3390/molecules27041275.